

Order Parameter Discovery for Quantum Many-Body Systems

Nicola Mariella,^{1,*} Tara Murphy,^{1,2,†} Francesco Di Marcantonio,^{3,‡} Khadijeh Najafi,^{4,§} Sofia Vallecorsa,^{5,¶} Sergiy Zhuk,^{1,**} and Enrique Rico^{3,5,6,7,††}

¹IBM Quantum, IBM Research Europe - Dublin

²Cavendish Laboratory, University of Cambridge,

J.J. Thomson Avenue, Cambridge CB3 0HE, United Kingdom

³Department of Physical Chemistry and EHU Quantum Center,

University of the Basque Country UPV/EHU, Box 644, 48080 Bilbao, Spain

⁴IBM Quantum, IBM T. J. Watson Research Center, Yorktown Heights, New York 10598, USA

⁵European Organization for Nuclear Research (CERN), Geneva 1211, Switzerland

⁶Donostia International Physics Center, 20018 Donostia-San Sebastián, Spain

⁷IKERBASQUE, Basque Foundation for Science, Plaza Euskadi 5, 48009 Bilbao, Spain

Quantum phase transitions reveal deep insights into the behavior of many-body quantum systems, but identifying these transitions without well-defined order parameters remains a significant challenge. In this work, we introduce a novel approach to constructing phase diagrams using the vector field of the reduced fidelity susceptibility (RFS). This method maps quantum phases and formulates an optimization problem to discover observables corresponding to order parameters. We demonstrate the effectiveness of our approach by applying it to well-established models, including the Axial Next Nearest Neighbour Interaction (ANNI) model, a cluster state model, and a chain of Rydberg atoms. By analyzing observable decompositions into eigen-projectors and finite-size scaling, our method successfully identifies order parameters and characterizes quantum phase transitions with high precision. Our results provide a powerful tool for exploring quantum phases in systems where conventional order parameters are not readily available.

I. INTRODUCTION

Quantum phase transitions (QPTs) in many-body quantum systems pose considerable challenges for theoretical modeling and experimental observation. Unlike classical phase transitions, which are driven by thermal fluctuations, QPTs are induced by changes in external parameters like magnetic fields or pressure, resulting in alterations to the ground state properties of a system.

Various methods have been developed to detect and characterize classical and quantum phase transitions. Among these is *Landau-Ginzburg theory* [1], designed to describe phase transitions and critical phenomena using a field theory description. Its formalism extends Landau's mean-field theory by constructing a free energy functional and accounting for spatial variations of the *order parameter*. The latter reflects the broken symmetry of the low-temperature phase.

While the theory above effectively describes phase transitions, studying QPTs in finite-size systems requires more sophisticated tools. This need arises from the *Kadanoff extended singularity theorem* [2, 3], highlighting the relevance of non-analytic behavior in thermodynamic quantities near the critical point.

Various methods, such as the *Renormalization Group* (RG) [4, 5] and *Finite-Size Scaling* (FSS) theory [6], have been developed to study QPTs in finite-size systems. RG operates by systematically removing less relevant degrees of freedom, highlighting the scale-independent features of a system. Thus, it provides insights into phase transitions by analyzing how physical systems behave across various length scales. This method involves coarse-graining the system and tracking the flow of coupling constants, with critical points emerging as fixed points of this flow.

FSS also investigates how physical quantities vary with the system size close to the critical point, facilitating the extraction of critical exponents from finite systems. Yet another approach involves employing machine learning techniques to detect phase transitions by identifying critical points and transition regions [7–11].

A specialized tool for detecting and characterizing phase transitions is the *quantum state fidelity* [12]. This concept, first applied to phase transitions in 1967 through the Anderson orthogonality catastrophe [13], measures the overlap between quantum states as system parameters change. *Fidelity susceptibility* [14, 15], a key concept in quantum information theory and quantum many-body physics, quantifies how sensitive a quantum state is to perturbations. It is particularly useful for detecting and characterizing quantum phase transitions, as it reveals sharp changes or singularities in fidelity near a quantum critical point, without relying on a design of tailored order parameters.

We describe the contributions of the present work. We extend the use of the fidelity susceptibility from previous studies (e.g. [14, 15]) and construct a vector field using a *reduced fidelity susceptibility* (RFS). We use the RFS

* nicola.mariella@ibm.com

† tm763@cam.ac.uk

‡ francesco.di.marcantonio@cern.ch

§ knajafi@ibm.com

¶ sofia.vallecorsa@cern.ch

** sergiy.zhuk@ie.ibm.com

†† enrique.rico.ortega@gmail.com

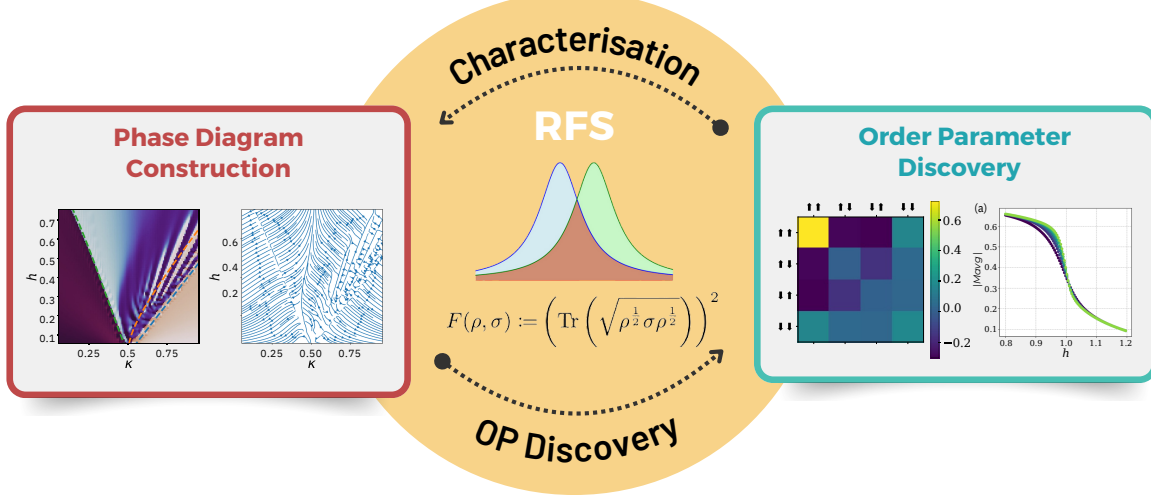


FIG. 1: Visualisation of the reduced fidelity susceptibility (RFS) uses. Here, we show that it can be used for both phase diagram construction of quantum systems and order parameter discovery.

for the qualitative classification of the different phases. As we will show, in the RFS vector field, sources appear as phase transitions, while sinks are representative of the ground states for the corresponding phases. In addition, we devise an optimization problem, which identifies observables representing order parameters from the RFS vector field. Specifically, we consider the class of order parameters determined by the expectation of a Hermitian observable (e.g., magnetization). Such an observable is optimized using data from the RFS. The order parameter discovery gives a quantitative description of the critical point. A schematic picture of our method can be seen in Figure 1.

We demonstrate the efficacy of the proposed method on detecting QPT for three different models: (i) axial next-nearest neighbor Ising (ANNNI) model [16, 17] (due to its phase diagram), (ii) the cluster Hamiltonian model (due to its non-local description), and (iii) a physically motivated example given by a Rydberg atomic quantum simulator. In all the above models, the proposed approach allows us to capture intricate details, such as the structure of ANNNI's floating phase or the string order parameter in the cluster model. For (iii), we discover additional features that were not identified by prior studies: specifically, we observe ripple-like features at high values of the parameters swept, which might suggest the presence of a more complex phase, yet an open question previously discussed in [18–20].

In summary, our mathematical framework establishes the phase diagram and enables the discovery of the order parameters for a Hamiltonian model, facilitating the understanding of different phases. We stress that our method can provide efficient certification and verification processes for quantum simulations and phase transition detection [21] and circumvents the need for full tomography of the wave function, relying instead on the reduced

density matrix to capture the relevant characteristic thermodynamic information.

The outline of the paper is as follows. In Section II we outline the notation used in the paper and introduce the concept of fidelity and the RFS. This is followed by Section III, where we outline the mathematical framework, introduce the RFS vector field, and highlight its potential to be used to detect phase transitions. In Section IV, we highlight how the aforementioned mathematical framework can be used to determine an order parameter for a given quantum system. We showcase this in Section V by using the above framework to construct the phase diagram for the ANNNI model, the cluster Hamiltonian, and a one-dimensional Rydberg chain, and demonstrate the ability to discover new order parameters. We end with a discussion of applications of this framework in Section VI and potential use cases for future work.

II. PRELIMINARY

We begin by defining the set of Hermitian matrices of order n , which is denoted by $\mathcal{S}_n := \{M \in \mathbb{C}^{n \times n} | M = M^\dagger\}$. We denote the identity matrix of order n by \mathbb{I}_n and the i th canonical basis vector for the vector space \mathbb{C}^n by \mathbf{e}_i .

Next, we introduce the concept of fidelity. Fidelity measures the similarity between two quantum states, and all its definitions embody the probability of distinguishing one quantum state from another.

Given mixed-states ρ, σ we define the *Uhlmann-Jozsa*

fidelity [12] by¹

$$F(\rho, \sigma) := \left(\text{Tr} \left(\sqrt{\rho^{\frac{1}{2}} \sigma \rho^{\frac{1}{2}}} \right) \right)^2, \quad (1)$$

which, for the remainder of the work, will be referred to as *fidelity*, unless otherwise specified. The latter definition of fidelity is not unique, indeed, Jozsa [12] obtained an axiomatic definition for a family of such functions. However, the Uhlmann fidelity stands for its unique relation to the *Bures distance*

$$d_B^2(\rho, \sigma) := 2 \left(1 - \sqrt{F(\rho, \sigma)} \right), \quad (2)$$

which is a quantification of the statistical distance between density matrices. A relevant result is the *Uhlmann theorem* [23], which expresses the fidelity in terms of the maximum overlap over all purifications of its arguments, that is

$$F(\rho, \sigma) = \max_{|\psi_\rho\rangle} |\langle \psi_\rho | \psi_\sigma \rangle|^2, \quad (3)$$

where $|\psi_\sigma\rangle$ and $|\psi_\rho\rangle$ denote some purifications of σ and ρ , respectively.

Following our discussion on the fidelity, we next consider a generic many-body parametric Hamiltonian $H(\lambda) = H_0 + \lambda H_I$, with eigenvalue equation $H(\lambda) |\psi_k(\lambda)\rangle = E_k(\lambda) |\psi_k(\lambda)\rangle$, where the index $k = 0$ identifies the ground state. For clarity, we may omit the dependence of the various objects from the parameter λ , when it does not result in ambiguity. In a perturbative approach w.r.t. a small parameter δ , the Taylor expansion for the fidelity reads

$$|\langle \psi_0(\lambda) | \psi_0(\lambda + \delta) \rangle| = 1 - \frac{1}{2} \mathcal{X}_F(\lambda) \delta^2 + O(\delta^3), \quad (4)$$

with the leading term (second-order) revealing the *fidelity susceptibility* \mathcal{X}_F (susceptibility for short) [15]. We note that the first-order term vanishes since the fidelity reaches a maximum at $\delta = 0$ for any λ . Informally, fidelity susceptibility quantifies how much the fidelity (or overlap) between two nearby states changes concerning a small change in a parameter (such as an external field or coupling strength) that defines the states. Let $\rho_0(\lambda) = |\psi_0(\lambda)\rangle \langle \psi_0(\lambda)|$ be the density matrix for the ground state of $H(\lambda)$. Two well-known formulations for the susceptibility² are given as;

$$\mathcal{X}_F(\lambda) = - \frac{\partial^2 \sqrt{F(\rho_0(\lambda), \rho_0(\lambda + \delta))}}{\partial \delta^2} \Big|_{\delta=0} \quad (5a)$$

$$= \lim_{\delta \rightarrow 0} - \frac{2 \ln \sqrt{F(\rho_0(\lambda), \rho_0(\lambda + \delta))}}{\delta^2}, \quad (5b)$$

where F is generalized to the Uhlmann fidelity in (1), when the arguments are not pure states. The expansion for the ground state of the perturbed Hermitian³ $H(\lambda)$ is given as;

$$|\psi_0(\lambda + \delta)\rangle \approx |\psi_0(\lambda)\rangle + \delta \sum_{k \neq 0} \frac{K_{k,0}}{E_k - E_0} |\psi_k(\lambda)\rangle, \quad (6)$$

where $K_{k,0} := \langle \psi_k(\lambda) | H_I | \psi_0(\lambda) \rangle$. This leads to another well-known formulation for the susceptibility

$$\mathcal{X}_F(\lambda) = \sum_{k \neq 0} \frac{|\langle \psi_k(\lambda) | H_I | \psi_0(\lambda) \rangle|^2}{(E_k - E_0)^2} \geq 0. \quad (7)$$

As noticed in [25], the latter, which depends solely on the spectrum, shows that the quantity \mathcal{X}_F is non-negative and diverges when the energy gap closes.

III. PHASE DIAGRAM CONSTRUCTION

Building upon the previous section's exploration of fidelity susceptibility, we next introduce the reduced fidelity susceptibility (RFS) vector field concept. In doing so, we consider a general many-body Hamiltonian parameterized by the space $\mathcal{X} \subseteq \mathbb{R}^2$, of which its decomposition in terms of base and driving components reads

$$H(\boldsymbol{\lambda}) = H_0 + \lambda_1 H_1 + \lambda_2 H_2, \quad (8)$$

with control parameters $(\lambda_1 \ \lambda_2)^\top \in \mathcal{X}$. We anticipate that choosing the two-dimensional parameters space is convenient for the visual approach, but not fundamental. Let $|\psi_0(\boldsymbol{\lambda})\rangle \in \mathcal{H}$ denote the ground state of the Hamiltonian H evaluated at $\boldsymbol{\lambda} \in \mathcal{X}$, with \mathcal{H} denoting the underlying Hilbert space. The Hilbert space \mathcal{H} is assumed bipartite, that is $\mathcal{H} = \mathcal{H}_A \otimes \mathcal{H}_B$, for some subsystems A and B . In addition, we assume the ground state is non-degenerate. Let $\rho_0(\boldsymbol{\lambda})$ denote the reduced density matrix (RDM) resulting from tracing out the subsystem B for the ground state, so

$$\rho_0(\boldsymbol{\lambda}) = \text{Tr}_B (|\psi_0(\boldsymbol{\lambda})\rangle \langle \psi_0(\boldsymbol{\lambda})|). \quad (9)$$

We consider a perturbative action in the parameter space and define

$$f(\boldsymbol{\lambda}, \boldsymbol{\delta}) = \sqrt{F(\rho_0(\boldsymbol{\lambda}), \rho_0(\boldsymbol{\lambda} + \boldsymbol{\delta}))} \in [0, 1], \quad (10)$$

for $\boldsymbol{\lambda} \in \mathcal{X}$ and $\boldsymbol{\delta}$ a perturbation in the latter space, where F is the fidelity defined in (1). As a consequence of the Uhlmann theorem (3), since the fidelity is the maximum over the overlap w.r.t. all purifications, then $f(\boldsymbol{\lambda}, \boldsymbol{\delta}) \geq |\langle \psi_0(\boldsymbol{\lambda}) | \psi_0(\boldsymbol{\lambda} + \boldsymbol{\delta}) \rangle|$, that is, the quantity in

¹ Some literature defines the fidelity in (1) as the square root of our F (e.g. [22]).

² The rightmost of (5a) is obtained by considering the Taylor expansion of $\ln(1 + x) = x - \frac{x^2}{2} + O(x^3)$, with $x = -\frac{1}{2} \mathcal{X}_F(\lambda) \delta^2 + O(\delta^3)$ from (4).

³ This result is commonly known as the Rayleigh–Schrödinger perturbation theory [24].

(10) is bounded below⁴ by the square root of the overlap between the perturbed ground states.

Following this, we introduce one of the key functions for our method⁵, that is

$$g(\boldsymbol{\lambda}) := - \left(\frac{\partial^2 f(\boldsymbol{\lambda}, \boldsymbol{\delta})}{\partial \delta_1^2} + \frac{\partial^2 f(\boldsymbol{\lambda}, \boldsymbol{\delta})}{\partial \delta_2^2} \right) \Big|_{\boldsymbol{\delta}=\mathbf{0}}. \quad (11)$$

We call the terms $\partial^2 f / \partial \delta_k^2$ the *reduced fidelity susceptibility* for the corresponding parameter λ_k . Indeed, it can be noted that the terms of the latter take the form of the fidelity susceptibility in (5a). Moreover, as shown in (7), the susceptibility is a non-negative quantity, then it is reasonable to consider a quantity resulting from the summation of susceptibilities for different directions (parameters). The adjective reduced is justified by the fact that we are considering RDMs instead of pure states as in (4). Similar forms of susceptibility have been considered in [27, 28]. We also note that for the regular susceptibility, it is clear that the linear term in the perturbative Taylor expansion of f vanishes for $\boldsymbol{\delta} = \mathbf{0}$. In [Appendix I](#) we expand on some key concepts in information geometry and its connection to the definition in (11).

We next obtain the vector field $P : \mathcal{X} \rightarrow \mathbb{R}^2$ (under sufficient smoothing assumptions) defined by;

$$P(\boldsymbol{\lambda}) := -\nabla_{\boldsymbol{\lambda}} g(\boldsymbol{\lambda}). \quad (12)$$

We stress that the gradient in (12) is expressed w.r.t. $\boldsymbol{\lambda}$ (parameters vector), whereas the Laplacian in (11) is related to $\boldsymbol{\delta}$ (perturbation). In addition, we obtain a scalar function mapping the parameters $\boldsymbol{\lambda}$ to the angles of the vectors in the image of P , that is

$$\theta(\boldsymbol{\lambda}) = \text{Arg}(\mathbf{e}_1^\top P(\boldsymbol{\lambda}) + i\mathbf{e}_2^\top P(\boldsymbol{\lambda})), \quad (13)$$

with $\text{Arg} : \mathbb{C} \rightarrow (-\pi, \pi]$ denoting the *principal argument*⁶. The latter is defined on the subset of the parameter space $\mathcal{X}' = \{\boldsymbol{\lambda} \in \mathcal{X} | P(\boldsymbol{\lambda}) \neq \mathbf{0}\}$. We note, as outlined in [Appendix H](#), the function in (13) is scale invariant in the proximity of QPT at $\boldsymbol{\lambda}_c$, that is $\theta((\boldsymbol{\lambda} - \boldsymbol{\lambda}_c)t) = \theta(\boldsymbol{\lambda} - \boldsymbol{\lambda}_c)$ for some small $t > 0$. The latter consideration is justified by the scaling behavior of fidelity susceptibility in the vicinity of QPT [29].

The function g defined in (11) corresponds to a notion of fidelity susceptibility. Moreover, the angle given by $\theta(\boldsymbol{\lambda})$ in (13) is the direction of the steepest decline in susceptibility. Consequently, we expect that phase transitions materialize as sources in the vector field (12), that

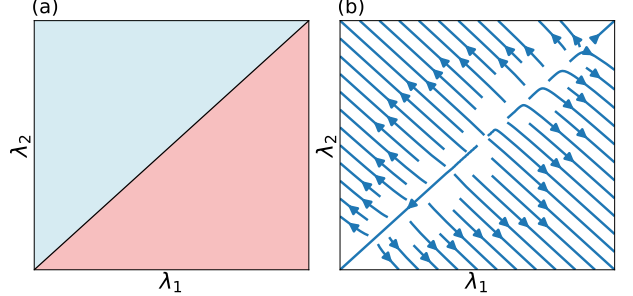


FIG. 2: (a) Color-mapped visualization of the fidelity vector field angle $\theta(\boldsymbol{\lambda})$. (b) Quiver plot of the vector field $P(\boldsymbol{\lambda})$ at a phase transition line. We note that the angle (thus the associated color) drastically changes at the phase transition in (a), which corresponds to a source (arrows radiate outward) in the vector field in (b).

is, the loci where the susceptibility is maximized. An example of this can be seen in [Figure 2](#). Furthermore, we note that the sinks are the points where the susceptibility reaches the local minimum. As the last step, if we map the co-domain of $\theta : \mathcal{X}' \rightarrow (-\pi, \pi]$ to a cyclic color map, we expect to obtain the phase diagram of the Hamiltonian in (8). This process is depicted in the sketch shown in [Figure 2](#), where in panel (a) we plot the angle $\theta(\boldsymbol{\lambda})$, and panel (b) represents the vector field with phase transition depicted by a diagonal line. Both panels suggest that in the proximity of a QPT, the gradient in (12) changes heading abruptly. We elaborate on this in [Appendix G](#). The practical implementation of the construction is expanded in [Appendix A](#).

We conclude with a remark on the complexity of the RDMs dimensions. We note that constant-size RDMs (relative to the system size) are particularly effective for detecting phase transitions characterized by local order parameters or short-range entanglement. This includes many conventional transitions, such as ferromagnetic and antiferromagnetic types, where critical behavior is governed by local observables or correlations extending over only a few sites. In phases with topological order or when non-local order parameters are needed to describe them, still non-linear functions of the RDM can characterize these phases.

IV. ORDER PARAMETER DISCOVERY

Following the results obtained in the preceding section, we next investigate whether it is possible to determine an order parameter that captures the phase transitions of a given Hamiltonian. Specifically, we consider the class of order parameters that are determined by the expectation of a Hermitian observable.

To answer this question, we apply the protocol as described in [Section III](#), and move from susceptibility-based identification of phases to determining the optimal ob-

⁴ Alternatively, this can be inferred by casting the partial trace as Kraus operator and by the monotonicity of the Uhlmann Fidelity [26].

⁵ Interestingly, we can obtain another function g proportional to that in (11) by considering f defined in terms of the squared Bures distance (2).

⁶ Let $z = x + iy$ with $x, y \in \mathbb{R}$, then the principal argument of z is defined by $\text{Arg}(x + iy) = \text{atan}2(y, x)$, with $\text{atan}2(y, x) = \lim_{c \rightarrow x^+} \arctan\left(\frac{y}{c}\right) + \frac{\pi}{2} \text{sign}(y) \text{sign}(x) (\text{sign}(x) - 1)$.

servable for distinguishing the phases, that is a *local order parameter*. A simpler method has been proposed in [30], where a Hermitian operator is optimized to distinguish two given RDMs. In the latter, the distinction is given by the sign of the expectation w.r.t. the optimal observable. Our contribution instead, aims at mimicking the behaviour of order parameters.

We first note that the function $\theta(\boldsymbol{\lambda}) \in (-\pi, \pi]$ in (13) represents the point-wise angle of the vector field (12). Also as argued before, phase transitions are likely to materialize as sources, and we assume that adjacent phases are distinguished by π radian angles. In other words, if the parameter $\boldsymbol{\lambda}_c \in \mathcal{X}$ is proximal to a critical point (for some Hamiltonian), and $\boldsymbol{\delta}$ a perturbation in the same space, then the assumption is that the corresponding gradient vectors have opposite directions, that is $|\theta(\boldsymbol{\lambda}_c) - \theta(\boldsymbol{\lambda}_c + \boldsymbol{\delta})| \approx \pi$. Consequently, there exists an optimal angle η such that

$$|\sin(\theta(\boldsymbol{\lambda}_c) + \eta) + \sin(\theta(\boldsymbol{\lambda}_c + \boldsymbol{\delta}) + \eta)| \approx 0. \quad (14)$$

Consider a parametric Hamiltonian on n spins with ground state RDM $\rho_0(\boldsymbol{\lambda})$ defined as in (9). In addition, we assume that the RDM is small enough to be handled classically. Given a finite set of parameters $\{\boldsymbol{\lambda}_i\}$ in the neighbourhood of $\boldsymbol{\lambda}_c$, we define a label $y_i \in [-1, 1]$ for each parameter $\boldsymbol{\lambda}_i$ as $y_i = \sin(\theta(\boldsymbol{\lambda}_i) + \eta)$. From (14), we see that distinct phases will be assigned opposite signs, $\text{sign}(y_i)$. We define the index sets $I^+ = \{i | y_i > 0\}$ and $I^- = \{i | y_i < 0\}$, partitioning the indices for the parameters $\{\boldsymbol{\lambda}_i\}$ determining the ground states laying on the ordered and disordered phases, respectively. Under the assumption of non-degeneracy of the problem (see Appendix B for more details), we devise the following (non-convex) *quadratically constrained quadratic program* (QCQP) [31],

$$\begin{aligned} \min_{M \in \mathcal{S}_m} \quad & \sum_{(i,j) \in I^+ \times I^-} \left(-\frac{\langle M \rangle_i^2}{p_i} + \frac{\langle M \rangle_j^2}{p_j} \right), \\ \text{s.t.} \quad & \|M\|_F^2 \leq 1, \end{aligned} \quad (15)$$

with $\langle M \rangle_i := \text{Tr}(\rho_0(\boldsymbol{\lambda}_i)M)$ defining the expectation of M at $\boldsymbol{\lambda}_i$, and $p_i := \text{Tr}(\rho_0(\boldsymbol{\lambda}_i)^2)$ the purity of the same RDM. We denoted by \mathcal{S}_m the set of Hermitian matrices of order m , which is also the order of the RDM $\rho_0(\boldsymbol{\lambda}_i)$.

This is commonly known in optimization literature as the *trust region problem* [32], which can be interpreted as a generalization of the minimum eigenvalue problem. The problem is solvable efficiently (polynomial time) even in the cases where the quadratic term is not positive semidefinite (i.e. non-convex) [33].

Informally, the optimization favors the non-zero expectation $\langle M \rangle_i$ for the labels $y_i > 0$ (ordered phase), whereas the quadratic term $\langle M \rangle_i^2$ penalizes non-zero expectations for the labels $y_i < 0$ (disordered phase). In essence, this mechanism is mimicking the order/disorder behavior of the order parameters, for all pairs of opposing (w.r.t. phase) RDMs $(\rho_0(\boldsymbol{\lambda}_i), \rho_0(\boldsymbol{\lambda}_j))$, with $(i, j) \in I^+ \times I^-$.

A special case of the problem in (15) arises when we consider the reference density matrices ρ_+ and ρ_- , each representing a phase (i.e. ordered vs disordered). The formulation becomes

$$\begin{aligned} \min_{M \in \mathcal{S}_m} \quad & -\frac{\text{Tr}(\rho_+ M)^2}{\text{Tr}(\rho_+^2)} + \frac{\text{Tr}(\rho_- M)^2}{\text{Tr}(\rho_-^2)}, \\ \text{s.t.} \quad & \|M\|_F^2 \leq 1. \end{aligned} \quad (16)$$

In Appendix C, it is shown that the objective of the latter is the quadratic form of an operator connected to the *Gram-Schmidt process* (GS) [34] – a method related to the *QR decomposition* in linear algebra. For a density matrix ρ , we define $\widehat{\rho} := \rho / \|\rho\|_F$ its associated norm-1 PSD (positive semidefinite⁷). Also, for Hermitian matrices A, B of the same order, we denote by $\langle A, B \rangle$ their Frobenius inner product. The special formulation leads to the close form solution

$$M = \frac{\widehat{\rho}_+ - \langle \widehat{\rho}_+, \widehat{\rho}_- \rangle \widehat{\rho}_-}{\sqrt{1 - \langle \widehat{\rho}_+, \widehat{\rho}_- \rangle^2}}, \quad (17)$$

when $\rho_+ \neq \rho_-$. The solution is Hermitian as it is a real-linear combination of PSDs. One can immediately verify that $\text{Tr}(\rho_- M) = 0$, whereas

$$\text{Tr}(\rho_+ M) = \|\rho_+\|_F \sqrt{1 - \langle \widehat{\rho}_+, \widehat{\rho}_- \rangle^2} > 0, \quad (18)$$

as expected. Geometrically, the solution in (17) can be interpreted as subtracting from $\widehat{\rho}_+$ its projection on $\widehat{\rho}_-$, hence the resulting Hermitian is orthogonal to ρ_- and has a non-zero overlap with ρ_+ (when $\rho_+ \neq \rho_-$). Moreover, the latter provides an understanding of the general problem. Specifically, the objective in (15) corresponds to the sum of special objectives in (16), for all pairs of opposing indices $(i, j) \in I^+ \times I^-$.

In practical terms, we consider RDMs on a few sites, thus the quadratic optimization problem can be solved classically upon computation of the partial trace on the ground states. Experimental results are presented in Section VB and the details for the solution of the optimization are expanded in Appendix B.

We remark, as discussed in [35], that the order parameter need not be unique, and any scaling operator that is zero in the disordered phase and non-zero in an adjacent (on the phase diagram), usually ordered phase, is a possible choice for an order parameter.

⁷ That is, a Hermitian matrix with non-negative eigenvalues.

V. EXPERIMENTS

To demonstrate the potential of the fidelity vector field in identifying QPTs and their corresponding order parameters, we apply our above methods to the cluster Hamiltonian and ANNNI models.

A. The ANNNI model

We first focus on the ANNNI Model [17, 36, 37], a theoretical model commonly used in condensed matter physics to study the behavior of magnetic systems. The Hamiltonian of such a system can be written as

$$H = -J_1 \sum_{i=1}^{N-1} \sigma_i^x \sigma_{i+1}^x - J_2 \sum_{i=1}^{N-2} \sigma_i^x \sigma_{i+2}^x - B \sum_{i=1}^N \sigma_i^z, \quad (19)$$

which we can rewrite in terms of the dimensionless ratios $\kappa = -J_2/J_1$ and $h = B/J_1$. The former is called the *frustration parameter* while the latter is related to the transverse magnetic field. With respect to the general Hamiltonian in (8), the parameters λ_1, λ_2 are now associated respectively to the parameters κ, h in (19).

In this model, spins are arranged in a one-dimensional lattice, with each spin existing in either the $|\uparrow\rangle$ or $|\downarrow\rangle$ state. The inclusion of the nearest neighbor and next-nearest-neighbor interactions in this model introduces a type of frustration, where the optimal alignment of neighboring spins is hindered due to competing interactions. The transverse field present, which represents an external magnetic field perpendicular to the direction of the spins, also induces quantum effects and modifies the overall behavior of the system. It is the combination of these complex interactions, which combine the effect of quantum fluctuations (owing to the presence of a transverse magnetic field) and frustrated exchange interactions that lead to phenomena such as quantum phase transitions. As a consequence, it is a paradigm for the study of competition between magnetic ordering, frustration, and thermal disordering effects [38].

The phase diagram can be seen in Figure 3, where three phase transitions are present. The first is the Ising-like transition between the Ferromagnetic (FM) and Paramagnetic (PM) phases, the second is the Kosterlitz-Thouless (KT) transition between the paramagnetic and floating phase (FP), and the final is the Pokrovsky-Talapov (PT) phase transition between the floating phase and antiphase (AP).

For more information on each of these phases and the corresponding phase transitions and their ground states see Appendix F.

Using the formalism as outlined in Section III, we first obtain the ground states of the Hamiltonian using the density matrix renormalization group (DMRG). Next, we consider a two-site RDM and calculate the RFS vector field and its corresponding angles. For details on how the

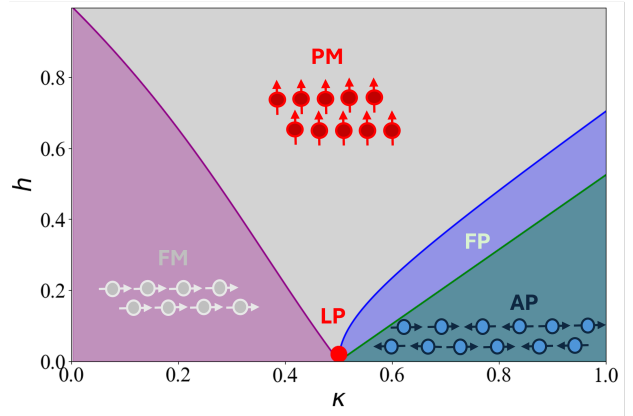


FIG. 3: (a) Phase Diagram of one-dimensional ANNNI Model. Here the pink represents the Ferromagnetic Phase (FM), where all spins are aligned along the x direction. The grey area corresponds to the paramagnetic phase (PM), in which the magnetic field dominates and all spins align along the z direction. The antiphase (AP) corresponds to the green region where the ground state takes the form of a staggered magnetization pattern with period four. Both the PM and AP are separated by the floating phase (FP). Here the spin chain can be seen as a ladder of two spin chains as sketched in the cartoon spin configurations.

RDM was obtained or the DMRG algorithm, see Appendix E. In Figure 4 (a), we plot the color-mapped angle as given in (13), as well as the numerical estimation for the Ising, KT, and PT phase transition lines, obtained in [8, 39, 40] (additional details given in Appendix F). There is a noticeable overlap between our approach and the literature. However, we cannot expect a perfect overlap, because of the finite-size scaling effects. As predicted in the method formulation, we have numerical confirmation from the vector field plotted in Figure 4 (b), that sources indeed correspond to phase transitions. This source and sink-like behavior, as seen in Figure 4 (b) corresponds to local maxima and minima of the RFS in (11) and is further analyzed in Appendix G.

Additionally, it is worth noting that the fidelity vector field surpasses previous simulations in its ability to capture intricate details that were previously unresolved in the floating phase [41]. Distinct ripples-like features are present, with the sources of the vector field corresponding to each of these structures indicating the presence of the phase transition between the paramagnetic and floating phases, specifically the KT transition. Future work will aim to explore the structure and fully utilize the potential of the RFS vector field in analyzing such complex phenomena. In the subsequent section, we demonstrate how we apply this method to determine order parameters for a given quantum system.

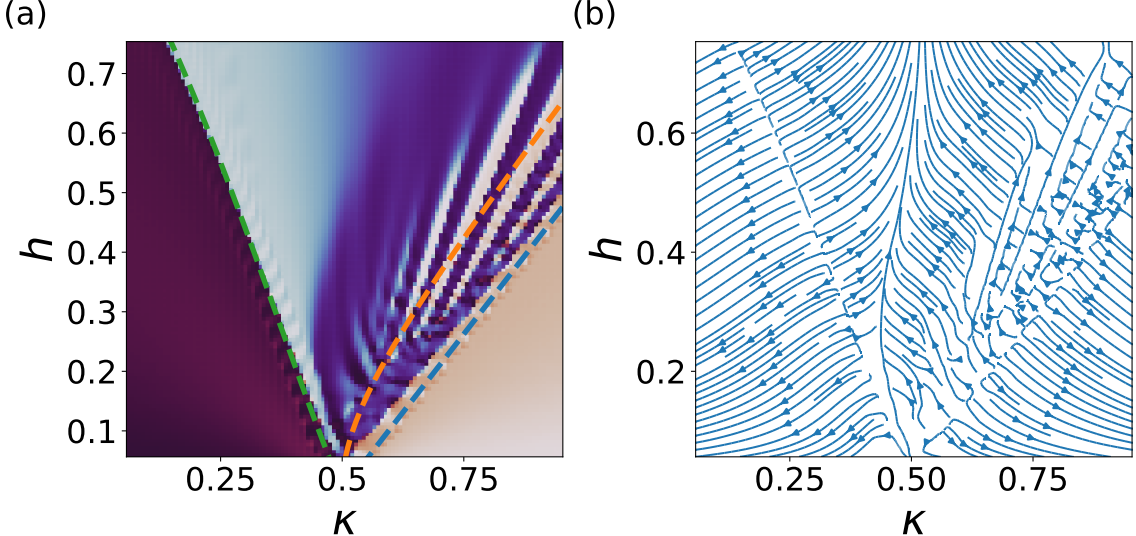


FIG. 4: Phase Diagram obtained using the reduced fidelity susceptibility of the one-dimensional ANNNI Model. Here a chain length of $L = 50$ spin sites was used and a two-site RDM was used when calculating the gradient of the reduced fidelity susceptibility. (a) The angle of the vector field given in (13) is plotted (b) the vector field given in (12) is plotted.

B. Order parameters discovery

Next, we experimentally demonstrate the validity of the method used for order parameter discovery (Section IV), and in doing so, propose a method for understanding the structure of the optimal observable. We proceed with the ANNNI model (19) by considering the phase diagram in the region $(\kappa, h) \in \mathcal{R} = [0.5, 2.1] \times [0, 1.6]$ and begin with the use of the RDMs of single spin sites. In other words, we focus on the side of the diagram (see Figure 3) that lies on the right of the vertical line through the Lifschitz point at $h = 0, \kappa = 0.5$. Let M denote the optimal observable for the order parameter discovery problem in (15), where the details concerning its solution are expanded in Appendix B. Optimizing for a single site observable, we find that $M \approx \mathbb{I} - \sigma_x$, which can be interpreted as magnetization. While this observable could be used as an order parameter for the Ising-like transition, highlighted in green in Figure 4, it failed to detect other transitions present in the ANNNI model, including the KT and PT transitions, highlighted orange and blue in Figure 4 respectively. As a result, to capture more transitions one must make use of Section IV and instead uncover a multi-site observable to detect all phase transitions present.

For this, we expand our RDM to the two middle spin sites of the chain of length L . The objective is to obtain the order parameters for the paramagnetic and the anti phases, which is highlighted in Figure 4, where we plot the result for the phase diagram construction (Section III) concerning the region \mathcal{R} , of which was obtained in the previous section using the RFS vector field.

In Figure 5 (a) we present the expectations of the observable M applied to the RDMs $\rho_0(\kappa_i, h_i)$, for a finite lattice of parameters $\{(\kappa_i, h_i)\}$, following the optimization process of obtaining a relevant order parameter M for this phase transition. We note that in the optimization process, the entire region, $(\kappa, h) \in \mathcal{R} = [0.0, 2.1] \times [0, 1.6]$, was used, which included all phase transitions present.

To understand the structure of the obtained observable, we next perform the eigendecomposition of M , that is

$$M = \sum_{i=1}^m \alpha_i M^{(i)} \quad (20)$$

where $M^{(i)}$ are rank-1 projectors and α_i the corresponding eigenvalues. Let $|\varphi(\theta)\rangle = \cos(\theta)|0\rangle + \sin(\theta)|1\rangle$, we define the parametric Hermitian $B(\theta_1, \theta_2)$ as

$$B(\theta_1, \theta_2) := |\varphi(\theta_1)\rangle \langle \varphi(\theta_1)| \otimes |\varphi(\theta_2)\rangle \langle \varphi(\theta_2)|. \quad (21)$$

Such an operator can be interpreted as the orthogonal projector (which is defined as a square matrix P such that $P^2 = P = P^\dagger$) generated by the state $|\uparrow\uparrow\rangle$, where the angles of the spins are θ_1 and θ_2 , respectively.

The component corresponding to the eigenvalue with the greatest magnitude is the projector $M^{(1)} = B(\theta_1, \theta_2)$ with $\theta_1 \approx 0.095\pi$ and $\theta_2 \approx 0.034\pi$, that is $M^{(1)} \approx |\uparrow\uparrow\rangle \langle \uparrow\uparrow|$. In Figure 5 (c), we plot the expectation of the observable $M^{(1)}$. A comparison with the plot in Figure 5 (a), shows that this is the main component for the paramagnetic phase.

The component $M^{(4)}$, with $\langle M^{(4)} \rangle$ depicted in Figure 5 (b), can be interpreted as the complementary to $M^{(1)}$.

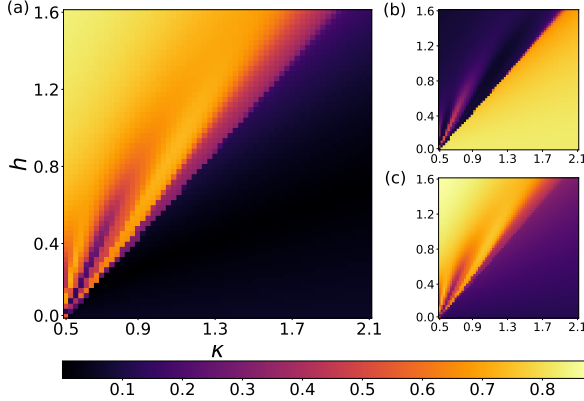


FIG. 5: Experiments for the order parameter discovery on the ANNNI model. Here a chain length of $L = 50$ spin sites was used and a two-site RDM was used when calculating the gradient of the reduced fidelity susceptibility. (a) Expectation of the optimal observable M for the paramagnetic phase. The expectations for the projectors $M^{(1)}$ and $M^{(4)}$ of (20), are respectively in (c) and (b).

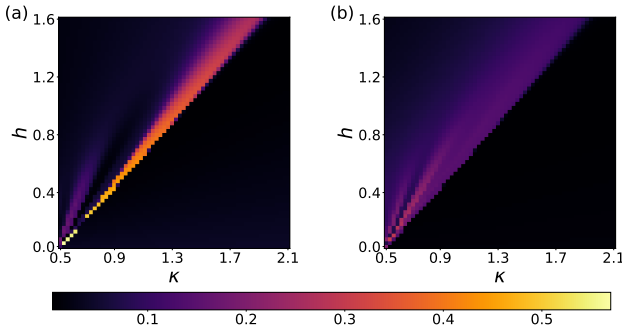


FIG. 6: Expectations of the projectors $M^{(3)}$ (a) and $M^{(2)}$ (b) revealing the floating phase. Here a chain length of $L = 50$ spin sites was used and a two-site RDM was used when calculating the gradient of the reduced fidelity susceptibility.

The operator approaches the following form

$$M^{(4)} \approx \frac{1}{4} (\mathbb{I}_2^{\otimes 2} + \sigma_x^{\otimes 2}) (\mathbb{I}_2^{\otimes 2} - \sigma_z^{\otimes 2}) = |\Psi^+\rangle\langle\Psi^+|, \quad (22)$$

with $|\Psi^+\rangle = (|\uparrow\downarrow\rangle + |\downarrow\uparrow\rangle)/\sqrt{2}$ (Bell's state), so the ordered phase for $M^{(4)}$ is the antiphase. This can be justified by the modulated structure of the antiphase $|\cdots \leftarrow \leftarrow \rightarrow \rightarrow \cdots\rangle$ (see [Appendix F](#) for a comprehensive introduction to ANNNI). Indeed we see that $\text{Tr}(M^{(4)}|\varphi\rangle\langle\varphi|) \neq 0$ for $|\varphi\rangle = |\leftarrow\rangle$ and $|\varphi\rangle = |\rightarrow\rangle$, whereas $\text{Tr}(M^{(4)}|\uparrow\uparrow\rangle\langle\uparrow\uparrow|) = 0$ (paramagnetic).

The remaining two components of the decomposition in (20) reveal an interesting structure. The third eigen-

vector determines the projector $M^{(3)} = B(\theta_1, \theta_2)$ with $\theta_1 \approx 0.381\pi$ and $\theta_2 \approx -0.331\pi$. Its expectation depicted in [Figure 6](#) (a), appears to highlight a section of the floating phase. The last projector $M^{(2)}$, whose details are omitted, produces another detail of the floating phase, which is depicted in [Figure 6](#) (b).

C. Finite Size Scaling

Next, we validate that the obtained observable M ([Section V B](#)) is indeed an order parameter for the ANNNI Model. We accomplish this by applying finite-size scaling and verifying that the critical exponents match those expected for the Ising-like universality class. Finite-size scaling is a technique used to study phase transitions by examining how physical quantities change with system size. It involves scaling the system size and observing how properties such as critical exponents converge to their thermodynamic limits as the size increases. By applying this method, we can extrapolate results obtained from finite systems to infer behavior in the infinite system limit. To demonstrate this phenomena we thus analyze the impact of chain length at the Ising-like transition. We again use the RDM ρ_L for two spin sites, which are related to the sites $\{L/2, L/2 + 1\}$, assuming L (linear size) is an even positive integer. We calculate the expectations of the observable M with the reduced density matrices $\rho_L(\kappa, h_i)$ with $\kappa = 0.001$ and $h \in [0.8, 1.2]$. In this parameter range, we can consider the next-nearest-neighbor interaction as a perturbation of the Ising model. Consequently, we anticipate observing the critical exponents characteristic of the 1D quantum Ising model.

If the observable M indeed functions as an order parameter, it should satisfy the following scaling relation for the chain length L [42]:

$$\max_h \left\{ \frac{\partial \langle M \rangle}{\partial h} \right\} = a'' L^{1/\nu} \left(1 + b'' L^{-\theta/\nu} \right), \quad (23)$$

where a'' and b'' are constants, and θ represents the exponent of an irrelevant parameter. As first step for the validation of the latter hypothesis, in [Figure 7](#) we plot the expectation (with observable M) and its derivative, for various chain lengths L .

For the 1D quantum Ising model, where $\nu = 1$, the maximum of the gradient should show a linear dependence on the chain length. To validate this, we plot the maximum gradient (i.e. the peaks in [Figure 7](#) (b)) as a function of the chain length, as shown in [Figure 8](#). The observed linear relationship confirms that $\nu = 1$.

We then proceed to determine the irrelevant parameter exponent θ and show that this exponent remains positive as the chain length increases. Consequently, for large values of L , the contribution from this term becomes negligible. As $L \rightarrow \infty$, this term approaches zero, leaving us with the critical exponents of the Ising model.

We first rescale the function such that $a'' = 1$ and using gradient descent we fit for b'' and θ . This fit-

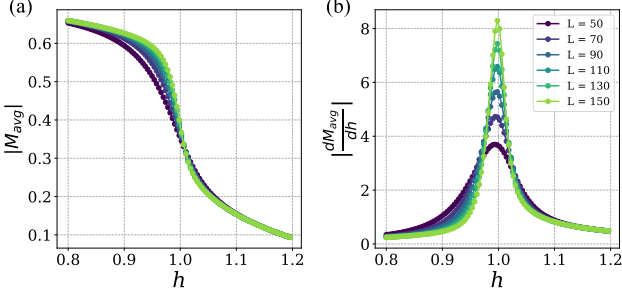


FIG. 7: The two-site observable obtained using the order parameter discovery framework (a) and its gradient with h (b) are applied to the ANNNI model's Ising-like transition for various chain lengths L . We set $\kappa = 0.001$ so that the next-nearest-neighbor term can be treated as a perturbation to the Ising model, which leads us to expect the system to belong to the Ising universality class.

ting process is illustrated in Figure 8 (b), where we plot $\frac{d\langle M \rangle}{dh} L^{-1}$. For irrelevant terms, we expect additional contributions to decay as L increases, which is indeed observed in Figure 8. By applying gradient descent to the obtained expectations for various lengths, we determine $\theta = 6.8 \times 10^{-5}$ and $b''/a'' = 1.0$. Consequently, the positive value of the correction term θ confirms that it is an irrelevant parameter.

To confirm that we belong to the Ising universality class, we fit the magnitude of the average observable near the critical point $h_c = 1.0$. In this regime, the critical magnetization should follow the relationship $M \propto |L|^{\beta/\nu}$. Assuming $\nu = 1.0$, we fit the values of the observed data and find $\beta = 0.123$, which is close to the expected value of $\beta = \frac{1}{8}$ for the Ising universality class.

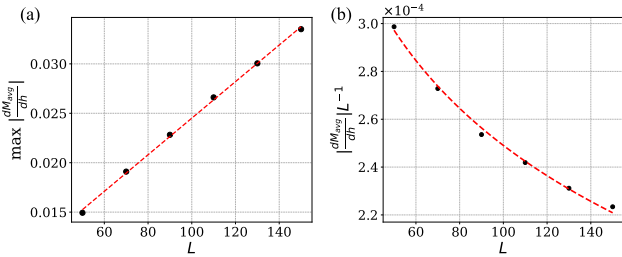


FIG. 8: (a) The maximum value of the gradient of the two-site observable obtained using the order parameter discovery framework. A linear relationship is observed, confirming that the system remains in the Ising universality class. (b) The irrelevant terms are plotted in (23). As the chain length L increases, an exponential decrease is observed, indicating that these terms approach zero as the system reaches the thermodynamic limit.

This analysis was also performed for the single-site observable $\mathbb{I} - \sigma_x$, and the critical exponent $\nu = 1$ was

consistently obtained. Therefore, near the Ising transition, it retains the critical exponents characteristic of the Ising model, accounting for finite-size scaling correction terms. Based on this analysis, we conclude that the obtained observable M functions as an order parameter.

D. The cluster Hamiltonian

Following the construction of the phase diagram for the ANNNI model, we next demonstrate the versatility of the fidelity vector field method by applying it to other models. Specifically, we apply the method described in Section III to the cluster Hamiltonian, defined by the Hamiltonian:

$$H = -h \sum_{i=1}^N \sigma_i^z - K \sum_{i=1}^{N-2} \sigma_i^x \sigma_{i+1}^z \sigma_{i+2}^x, \quad (24)$$

Concerning the general Hamiltonian in (8), the parameters λ_1, λ_2 are now associated with the parameters h, K . When the two parameters are equal, a phase transition is expected between a trivial phase (for $h > K$) and a Symmetry Protected Topological (SPT) phase (for $h < K$). To distinguish between these two phases, string order parameters (SOPs) are commonly used, as they can reveal hidden orders or symmetries within the system. In the case of the cluster Hamiltonian, the system exhibits certain symmetries, denoted by $G_{odd} = \prod_{k=0}^N Z_{2k+1}$ and $G_{even} = \prod_{k=0}^N Z_{2k}$.

From [43, 44], a general SOP can be expressed as

$$S_{\Sigma}^{O^L, O^R} = \lim_{|j-k| \rightarrow \infty} \left\langle \psi_0 \left| O^L(j) \left(\prod_{i=j+1}^{k-1} \Sigma_i \right) O^R(k) \right| \psi_0 \right\rangle \quad (25)$$

where ψ_0 is the state of the system, $\prod_{i=j+1}^{k-1} \Sigma_i$ (in our case G_{odd} or G_{even}) preserves the local symmetries of the system, and $O^{L/R}$ are appropriately chosen to detect the phase transition. In this particular system, a typical order parameter used for the phase transition is $\sigma^x \otimes \sigma^z \otimes I \otimes \sigma^z \otimes \sigma^x$, or another commonly used one is $\sigma^x \otimes \sigma^y \otimes \sigma^z \otimes \sigma^y \otimes \sigma^z$ as discussed in [45].

We begin by focusing on reconstructing the phase diagram as discussed in section Section III. To determine the ground states of the Hamiltonian, we employ DMRG, following the procedure described in Appendix E. We replicate the calculations outlined in Section VA to construct the phase diagram for the cluster Hamiltonian, which is presented in Figure 9. The phase transition is visible, with a distinct boundary separating the two phases.

Next, we turn our attention to identifying an order parameter for this phase transition by following the method described in Section IV. Using a five-site RDM, we derive an order parameter that effectively distinguishes between the different phases, as shown in 10.

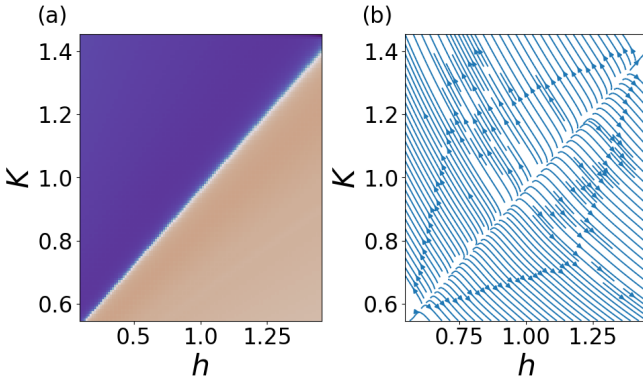


FIG. 9: Phase Diagram obtained using the reduced fidelity susceptibility of the one-dimensional cluster Hamiltonian where (a) the angle of the vector field given in (13) is plotted (b) the vector field given in (12) is plotted. We note that the phase transitions correspond to a source in the vector field.

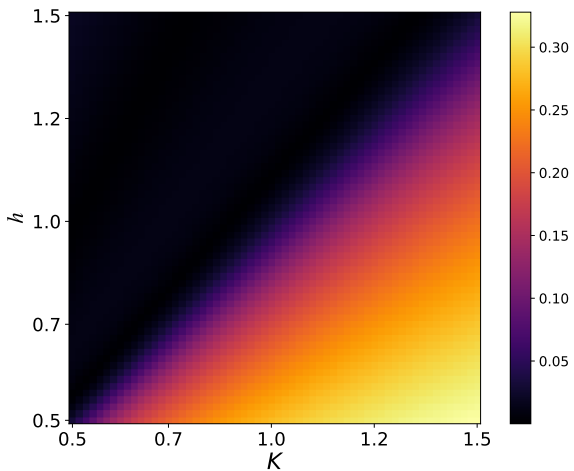


FIG. 10: Expectation of the optimal observable M for cluster Hamiltonian. Here a chain length of $L = 50$ spin sites was used and a five-site RDM was used when calculating the gradient of the reduced fidelity susceptibility.

Although this order parameter is a linear combination of various tensor products of Pauli operators, the two terms with the largest coefficients are $\sigma^x \otimes \sigma^z \otimes I \otimes \sigma^z \otimes \sigma^x$ and $\sigma^x \otimes \sigma^y \otimes \sigma^z \otimes \sigma^y \otimes \sigma^z$, both observables that reflect the symmetry of the SPT phase. This suggests that our observable has correctly identified the appropriate SOP and effectively exploited the system's symmetries to distinguish between the two phases.

It is worth noting that similar calculations were performed using different sizes of RDMs, specifically one and two sites. These attempts, however, failed to detect the phase transition, indicating that these smaller RDMs do not capture enough information about the phases on their own.

To conclude, we have demonstrated that the RFS vector field accurately reproduces the phase diagrams of both the ANNNI and cluster Hamiltonians, showcasing its robustness and reliability in capturing the phase transitions of diverse systems. Furthermore, we successfully identified an order parameter that leverages each system's symmetries to distinguish between different phases, further validating our approach.

E. The Rydberg model spin chain

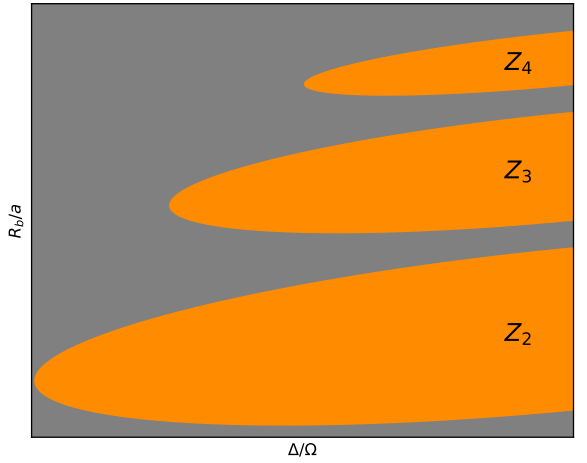


FIG. 11: Schematic of the phase diagram for the Rydberg Model as a function of the parameters $\frac{\Delta}{\Omega}$ and $\frac{R_b}{a}$ (see the main text for more details). The orange regions represent the emergence of various crystalline quantum phases with \mathbb{Z}_N order.

1. Model description

The Rydberg model is a quantum many-body system that has attracted considerable interest, particularly its role in experimental quantum simulation platforms [46–49]. The system is composed of a chain of atoms such that each atom can either remain in its ground state or be excited to a highly energetic Rydberg state, characterized by an electron occupying a very high orbital [50]. The model captures the dynamics of strongly interacting systems, as atoms in Rydberg states exhibit long-range dipole-dipole interactions, significantly affecting the system's collective behavior. Using these interactions, a variety of exotic quantum phases can be simulated, including quantum phase transitions and spin-liquid phases, making the Rydberg model an essential tool for probing non-equilibrium phenomena in quantum simulators [51].

Mathematically, the Rydberg model can be formulated as a spin-1/2 system, where each site of the chain represents an atom that can either be in the ground state

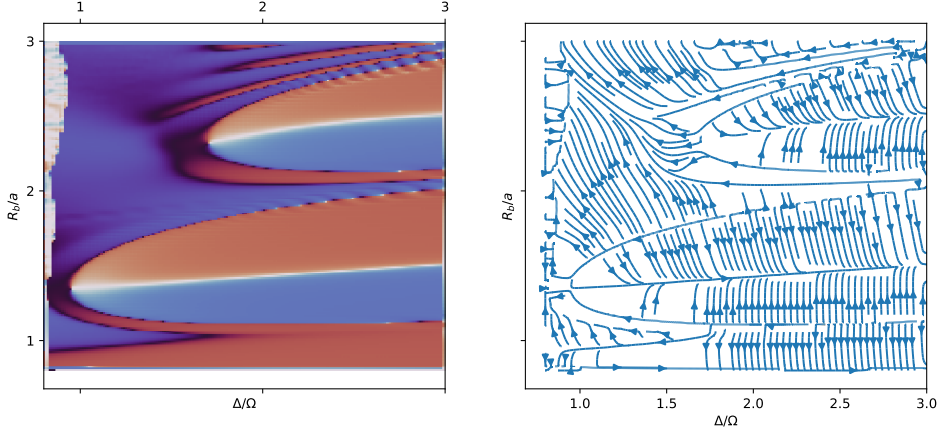


FIG. 12: Phase diagram for the Rydberg Model obtained with a one-site RDM from a chain of length $L = 50$, with long-range interactions truncated at the fourth nearest neighbor. The lower crystalline phase corresponds to the \mathbb{Z}_2 crystalline phase, while the upper corresponds to the \mathbb{Z}_3 crystalline phase.

(represented by the spin state $|0\rangle$) or in the Rydberg state (represented by the spin state $|1\rangle$). The Hamiltonian of the Rydberg model is typically expressed as

$$H = \Omega \sum_i \sigma_i^x - \Delta \sum_i n_i + \sum_{i < j} V_{ij} n_i n_j, \quad (26)$$

where σ_i^x is the Pauli-x matrix acting on-site i , and $n_i = |1\rangle \langle 1|_i$ is the number operator that projects onto the Rydberg state at site i . The parameters Ω and Δ represent the Rabi frequency and detuning, respectively, which control the driving field and energy offset of the system. The second term in the Hamiltonian describes the interaction between atoms in their Rydberg states, with $V_{ij}(r) \propto 1/r^6$ representing the strength of the interaction between atoms at sites i and j . For $\Delta > 0$, various spatially ordered phases emerge due to the competition between two effects: the detuning term, which favors a high population of atoms in the Rydberg state, and the Rydberg blockade, which prevents the simultaneous excitation of atoms that are closer together than the blockade radius R_b , where the interaction strength $V(R_b)$ is equal to the Rabi frequency Ω .

We define the distance between adjacent spins as a , thus $r = |i - j|a$, and we also define the Rydberg Radius as $V(R_b) = \Omega$. Thus the Hamiltonian can be rewritten accordingly;

$$H = \sum_i \sigma_i^x - \frac{\Delta}{\Omega} \sum_i n_i + \left(\frac{R_b}{a} \right)^6 \sum_{i < j} \frac{1}{|i - j|^6} n_i n_j, \quad (27)$$

It is the parameters $\frac{\Delta}{\Omega}$ and $\frac{R_b}{a}$ (which correspond to λ_1, λ_2 in the general case in (8)) that we will vary in the following section.

In the limit of strong interactions, the Rydberg blockade phenomenon becomes significant, where two neighboring atoms cannot both be excited to the Rydberg state due to the large energy cost. This constraint leads

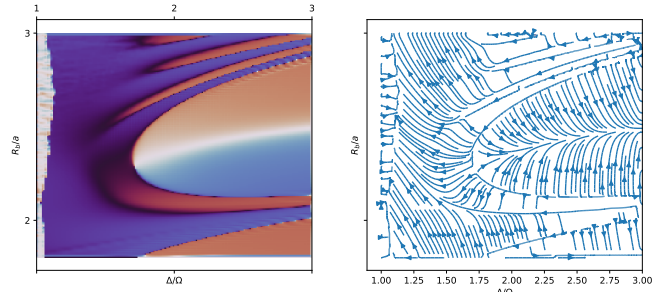


FIG. 13: Detail of the phase diagram for the Rydberg Model around the \mathbb{Z}_3 crystalline phase. Due to the high resolution of the phase diagram, ripple-like features can be observed, which signal a more complex phase to be determined.

to the emergence of various quantum phases, including crystalline phases with \mathbb{Z}_N symmetry (N being an integer), which are characterized by periodic arrangements of Rydberg excitations.

A schematic of the phase diagram is given in Figure 11.

2. Phase diagram construction

In previous studies, the phase diagram of the Rydberg model has been explored using various techniques such as entanglement entropy [18], machine learning methods [52], and fidelity [19]. We obtain the phase diagram, with the first result presented in Figure 12. Here, we particularly focus on the \mathbb{Z}_2 and \mathbb{Z}_3 crystalline phases, which are typically observed in this model (See Figure 13 for a closer look at the \mathbb{Z}_3 crystalline phase). We considered a chain of length $L = 50$, with long-range interactions truncated at the fourth nearest neighbor. The $1/r^6$ interaction term was approximated using an exponential

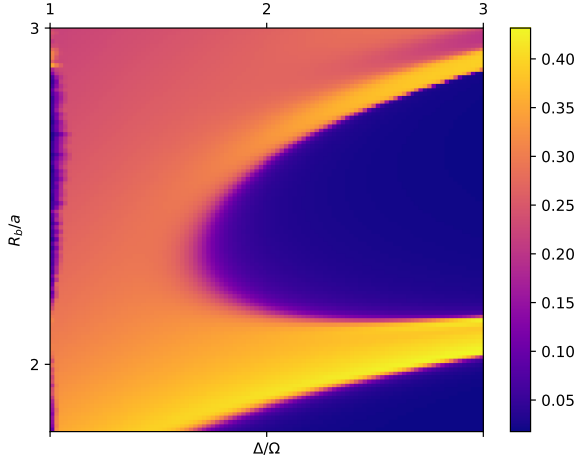


FIG. 14: Rydberg model – The expectation for a 1-site observable that highlights the disordered phase versus the crystalline phases \mathbb{Z}_2 and \mathbb{Z}_3 . Notably, the two crystalline phases cannot be distinguished using a 1-site observable.

form, as described in [53].

Our results are consistent with the parameter ranges for each crystalline phase in the phase diagram, as reported in previous studies [53]. However, a noteworthy observation is that our method captures additional features that were not identified by earlier approaches. Specifically, we observe ripple-like features at high values of the parameters swept, which may indicate the presence of a more complex phase - a topic previously discussed in [19, 20, 54]. Additionally, we identify a line within each crystalline phase corresponding to the minimum of the reduced fidelity susceptibility, or equivalently, the maximum of the fidelity.

Notably, due to the high resolution of our phase diagram, we once again observe ripple-like features, consistent with previous findings in [19].

3. Order parameters

Next, we focus on the determination of an order parameter to detect each of these phase transitions. We initially start with a one-site RDM to try to determine the different phases as seen in Figure 12. The projectors from the determined order parameter can be seen in Figure 14. As is evident that while it can determine the difference between the ordered and disordered phases, it fails to differentiate the different crystalline phases. Extending this to three sites results in the same projectors, which are unable to differentiate the different crystalline phases.

It is not until a four-site RDM is used that the different disordered phases, \mathbb{Z}_3 , \mathbb{Z}_2 can be characterized. This result is seen from the projectors of the observable in Figure 15.

Firstly, for the \mathbb{Z}_2 crystalline phase, the projector of the state $|0101\rangle$ is used to detect this phase, showing that the agreed state of alternating spin up and spin down is evident in this phase, agreeing with previous literature.

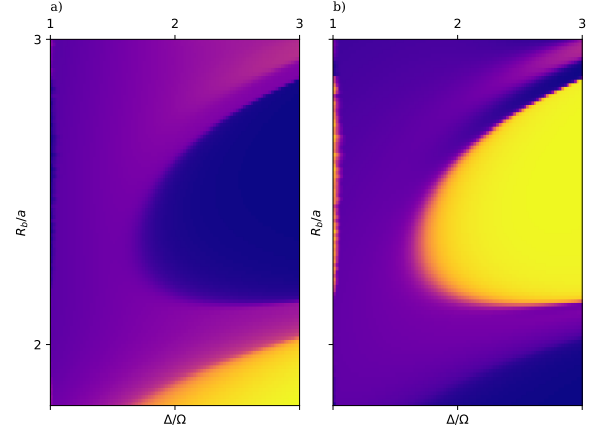


FIG. 15: Rydberg model – Highlights from the eigen decomposition of the order parameter on a 4-site RDM. The plots present the expectations of the projectors that reveal, respectively, the crystalline (a) \mathbb{Z}_2 and (b) \mathbb{Z}_3 phases.

Similarly, for the \mathbb{Z}_3 phase, the projector of the $|0001\rangle$ was determined from the order parameter, which is also in agreement with previous literature. Expanding the RDM to include additional sites would make this symmetry more evident.

VI. CONCLUSION

We have developed a novel and broadly applicable method for detecting quantum phase transitions based on reduced fidelity susceptibility (RFS), requiring only local reduced density matrices and no prior knowledge of symmetries, order parameters, or the nature of the transition. Applied to the axial next-nearest-neighbor Ising (ANNNI) model, our approach reveals subtle features of the phase diagram that elude conventional techniques, demonstrating both its sensitivity and efficiency. The RFS framework constructs a vector field that offers intuitive visual and conceptual access to phase structure, making it a powerful diagnostic for complex many-body phenomena. Looking forward, we aim to extend this method to systems exhibiting topological order—where traditional local order parameters fail—by exploiting its compatibility with non-linear functions of local reduced states (e.g., entanglement entropy) [55–57], thereby probing global quantum correlations through minimal local information.

Additionally, our framework demonstrates significant promise for application in quantum hardware environments. Utilizing the reduced density matrix thermodynamic information, it circumvents the need for full-

function tomography while still capturing essential characteristics of phase transitions.

Moreover, we extended our framework to devise a method for discovering order parameters in systems where they are unknown. The reversed method, applied to the ANNNI model, was validated through the decomposition and finite-size scaling of the identified order parameter. This validation underscores the framework's potential to explore and analyze novel systems, including unexplored phenomena such as floating phases in a quantum system. We believe that the proposed approach is an important milestone in phase transition detection and order parameter discovery, offering a robust tool for exploring the complex landscape of quantum systems.

VII. ACKNOWLEDGMENT

The data generated from quantum simulations and supporting this study are available from the authors upon reasonable request.

We are grateful to Dmytro Mishagli (IBM) and Victor Valls (IBM) for their valuable input and suggestions.

F.DM and E.R. acknowledge support from the BasQ strategy of the Department of Science, Universities, and Innovation of the Basque Government.

E.R. is supported by the grant PID2021-126273NB-I00 funded by MCIN/AEI/ 10.13039/501100011033 and by “ERDF A way of making Europe” and the Basque Government through Grant No. IT1470-22. This work was supported by the EU via QuantERA project T-NiSQ grant PCI2022-132984 funded by MCIN/AEI/10.13039/501100011033 and by the European Union “NextGenerationEU”/PRTR. This work has been financially supported by the Ministry of Economic Affairs and Digital Transformation of the Spanish Government through the QUANTUM ENIA project called – Quantum Spain project, and by the European Union through the Recovery, Transformation, and Resilience Plan – NextGenerationEU within the framework of the Digital Spain 2026 Agenda.

This work has been partially funded by the Eric & Wendy Schmidt Fund for Strategic Innovation through the CERN Next Generation Triggers project under grant agreement number SIF-2023-004.

Appendix A: Construction of the phase diagram

Starting from results devised in Section III, we proceed with the numerical construction of the phase diagram. We consider a rectangular region of the Hamiltonian parameters $\mathcal{R} \subseteq \mathcal{X}$. Given a step in the parameters space $h > 0$, we construct a finite lattice of parameters $\{\boldsymbol{\lambda}_{i,j}\} \subset \mathcal{R}$, such that

$$\lambda_{i+d_i, j+d_j} = \lambda_{i,j} + d_j h \mathbf{e}_1 + d_i h \mathbf{e}_2, \quad (\text{A1})$$

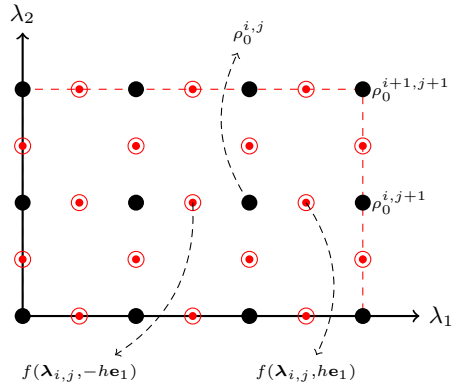


FIG. 16: Structure of the lattice of RDMs $\rho_0^{i,j} := \rho_0(\lambda_{i,j})$ induced by a finite lattice of parameters $\{\lambda_{i,j}\}$, contained in a region \mathcal{R} (outer rectangle).

with d_i, d_j belonging to a subset of \mathbb{Z} . Using the density matrix renormalization group (DMRG) [58, 59], we obtain the RDM related to the ground state (for a selected subsystem) for the parameter $\lambda_{i,j}$, which we define as $\rho_0^{i,j} = \rho_0(\lambda_{i,j})$, where the RHS is defined in (9). In Figure 16 the lattice points for the RDMs $\rho_0^{i,j}$ are represented by the symbol \bullet .

We proceed with the preparation of an approximation \tilde{g} of the function g , that is the RFS defined in (11). The latter is the Laplacian of the function $f(\boldsymbol{\lambda}, \boldsymbol{\delta})$ defined in (10). So, starting from the lattice of parameters $\{\boldsymbol{\lambda}_{i,j}\}$, we obtain the fidelity perturbations

$$f(\lambda_{i,j}, d_j h \mathbf{e}_1 + d_i h \mathbf{e}_2) = \sqrt{F} \left(\rho_0^{i,j}, \rho_0^{i+d_i, j+d_j} \right), \quad (\text{A2})$$

for a fixed step h (which defines the lattice of parameters) and $d_i, d_j \in \{-1, 0, 1\}$. We can immediately verify the computational advantage of the approach since adjacent lattice points share a fidelity perturbation. For example $f(\boldsymbol{\lambda}_{i,j}, h\mathbf{e}_1) = f(\boldsymbol{\lambda}_{i,j+1}, -h\mathbf{e}_1)$. In Figure 16, the fidelity perturbations are represented with the symbol \circledast and placed between adjacent lattice points to emphasize the concept of sharing. By considering the finite differences approximation of the second derivative⁸, and by noting that $f(\boldsymbol{\lambda}_{i,j}, \mathbf{0}) = 1$ (for all valid i, j), we obtain

$$\tilde{g}(\boldsymbol{\lambda}_{i,j}) = \frac{4 - \sum_{\boldsymbol{\delta} \in \Omega} f(\boldsymbol{\lambda}_{i,j}, \boldsymbol{\delta})}{h^2}, \quad (\text{A4})$$

where $\Omega = \{\pm h\mathbf{e}_1, \pm h\mathbf{e}_2\}$ is the set of perturbation displacements around $\lambda_{i,j}$. In practice, we omit the factor

⁸ For a function $f : \mathbb{R} \rightarrow \mathbb{R}$, under sufficient smoothing conditions, we make use of the following approximation

$$\frac{d^2 f}{dx^2} \approx \frac{f(x+h) + f(x-h) - 2f(x)}{h^2}, \quad (A3)$$

for some $h > 0$.

$1/h^2$ (numerically convenient) which is irrelevant for the subsequent computations. We proceed by adhering to the structure outlined in [Section III](#). Obtained the RFS approximation \tilde{g} , we continue with the computation of its gradient. Before that, we need to introduce a few concepts related to discrete signal processing.

For a continuous function $f : \mathbb{R}^2 \rightarrow \mathbb{R}^2$, we define the convolution at $(x, y) \in \mathbb{R}^2$ for discrete 2-dimensional signals as

$$f(x, y) * k := \sum_{i=-N}^N \sum_{j=-N}^N k(j, i) f(x - jh, y - ih), \quad (\text{A5})$$

where k is a convolution kernel with support N , that is $k(j, i) = 0$ for $|i| > N$ or $|j| > N$. Also, the scalar $h > 0$ represents the step for the lattice of points $\{(x y)^\top + (jh ih)^\top | i, j \in \mathbb{Z}\}$. We introduce a discrete differentiation operator called the *Sobel operator* [60] whose x component is given by the kernel matrix

$$G_x := \begin{pmatrix} -1 & 0 & 1 \\ -2 & 0 & 2 \\ -1 & 0 & 1 \end{pmatrix}. \quad (\text{A6})$$

The Sobel finds applications mainly in computer vision and it was initially developed to obtain an efficiently computable gradient operator with more isotropic characteristics than the Roberts cross operator [61].

Now, we define our kernel as $k = G_x + iG_x^\top$, which corresponds to the approximation of the gradient w.r.t. x on the real part and the y component on the imaginary part.

We obtain an equivalent approximation of P in [\(12\)](#) using the convolution

$$\tilde{P}(\boldsymbol{\lambda}_{i,j}) = -\tilde{g}(\boldsymbol{\lambda}_{i,j}) * k \quad (\text{A7a})$$

$$= -\sum_{a=-1}^1 \sum_{b=-1}^1 k(a, b) \tilde{g}(\boldsymbol{\lambda}_{i-a, j-b}) \in \mathbb{C}. \quad (\text{A7b})$$

When the indices (i, j) of the lattice elements are beyond the limits of definition we define $\tilde{g}(\boldsymbol{\lambda}_{i,j}) = 0$.

The first outcome of the process is a point-to-color graph

$$\boldsymbol{\lambda}_{i,j} \mapsto c \left(\text{Arg} \left(\tilde{P}(\boldsymbol{\lambda}_{i,j}) \right) \right), \quad (\text{A8})$$

where $c(\cdot)$ is a colormap which we introduce now. Let \mathcal{C} be a space of colors and let $c : (-\pi, \pi] \rightarrow \mathcal{C}$ be a mapping from the angle θ to a color in \mathcal{C} . The function c is required to be smooth on $(-\pi, \pi)$ and non-constant, also it must be such that $\lim_{\theta \rightarrow -\pi} c(\theta) = c(\pi)$. The latter point is fundamental for dealing with the discontinuity of $\text{Arg}(\cdot)$ in the non-positive real axis. Colormaps fulfilling the latter conditions are known as *cyclic* [62, 63]. In addition, the resulting signal is upsampled by factor 2 using an interpolation filter [64]. An example outcome obtained using the present procedure is reported in [Figure 4](#).

The final step of the diagram construction consists of the plotting of the vector field in [\(12\)](#). The approach makes use of the *Runge–Kutta method* [65] and our reference implementation is part of the function `matplotlib.pyplot.streamplot` of the software package `MATPLOTLIB` [63]. In the realm of differential equations, the Runge–Kutta method is a well-known algorithm for solving initial-value problems. In our instance, the velocities on the lattice $\{\boldsymbol{\lambda}_{i,j}\}$ are given by the gradient in [\(12\)](#). The initial values instead, are the points on the boundary of the lattice. Furthermore, a heuristic path of lattice points spiraling toward the center is added to the initial values, to improve the density of the streamlines.

Appendix B: Solution of the order parameter discovery problem

In this section, we expand on the solution of the order parameter discovery problem defined in [\(15\)](#). Instead, the special case in [\(16\)](#) is treated in [Appendix C](#). We restate the problem for clarity and convenience, so

$$\begin{aligned} \min_{M \in \mathcal{S}_m} \sum_{(i,j) \in I^+ \times I^-} \left(-\frac{\langle M \rangle_i^2}{p_i} + \frac{\langle M \rangle_j^2}{p_j} \right), \\ \text{s.t. } \|M\|_F^2 \leq 1, \end{aligned} \quad (\text{B1})$$

with $\langle M \rangle_i := \text{Tr}(\rho_0(\boldsymbol{\lambda}_i) M)$ and $p_i := \text{Tr}(\rho_0(\boldsymbol{\lambda}_i)^2)$.

We introduce the *row-major vectorization operator* $\text{vec}_r(\cdot) : \mathbb{C}^{n \times n} \rightarrow \mathbb{C}^{n^2}$ defined as

$$\text{vec}_r(M) := \sum_{i=1}^n M |i\rangle \otimes |i\rangle, \quad (\text{B2})$$

for any matrix M of order n in \mathbb{C} . For matrices A, B of order n we will be using the identity

$$\text{Tr}(AB^\dagger) = \text{vec}_r(A)^\dagger \text{vec}_r(B). \quad (\text{B3})$$

We recall that we denoted \mathcal{S}_m the set of Hermitians of order m in \mathbb{C} . We define the set of vectorized Hermitians of order m as

$$\widehat{\mathcal{S}_m} := \{\text{vec}_r(M) | M \in \mathcal{S}_m\}. \quad (\text{B4})$$

Let $\rho_i = \rho_0(\boldsymbol{\lambda}_i)$, and let I be some finite index set. Assume $M \in \mathcal{S}_m$, then we have that

$$\sum_{i \in I} \frac{\langle M \rangle_i^2}{p_i} = \sum_{i \in I} \frac{(\text{Tr}(\rho_i M))^2}{p_i} \quad (\text{B5a})$$

$$\stackrel{(\text{B3})}{=} \sum_{i \in I} \frac{(\text{vec}_r(M)^\dagger \text{vec}_r(\rho_i))^2}{p_i} \quad (\text{B5b})$$

$$= \mathbf{x}^\dagger \left(\sum_{i \in I} \frac{\mathbf{r}_i \mathbf{r}_i^\dagger}{p_i} \right) \mathbf{x}, \quad (\text{B5c})$$

with $\mathbf{x} := \text{vec}_r(M)$ and $\mathbf{r}_i := \text{vec}_r(\rho_0(\boldsymbol{\lambda}_i))$. We note that the vectors \mathbf{x} and \mathbf{r}_i belong to the set of vectorized Hermitians $\widehat{\mathcal{S}}_m$.

We use the result in (B5a) to rewrite the optimization problem in (15) in the equivalent⁹ form

$$\min_{\mathbf{x} \in \mathbb{C}^{m^2}} \mathbf{x}^\dagger A \mathbf{x}, \quad (\text{B6a})$$

$$\text{s.t. } \|\mathbf{x}\|_2^2 \leq 1, \quad (\text{B6b})$$

$$\mathbf{x} \in \widehat{\mathcal{S}}_m, \quad (\text{B6c})$$

with

$$A := -\frac{1}{|I^+|} \sum_{i \in I^+} \frac{\mathbf{r}_i \mathbf{r}_i^\dagger}{p_i} + \frac{1}{|I^-|} \sum_{j \in I^-} \frac{\mathbf{r}_j \mathbf{r}_j^\dagger}{p_j}. \quad (\text{B7})$$

This formulation confirms that the optimization is a quadratically constrained quadratic program as stated in Section IV. The matrix A (determined by data) is Hermitian, so the objective in (B6a) is real and well-defined (even in the absence of constraint (B6c)). We expand on the condition for the non-degeneracy of the problem introduced in Section IV. We impose that the matrix A is *indefinite* [66], where the Hermitian structure is fulfilled by the construction in (B7). In other words, we require the matrix A to have both (strictly) positive and negative eigenvalues¹⁰.

Let $(\cdot) \succcurlyeq (\cdot)$ denote the *Loewner order* [66], that is the partial order on the cone of PSD (positive semidefinite) matrices. Specifically, for any pair of Hermitian matrices X, Y we have that $X \succcurlyeq Y$ if and only if $X - Y$ is PSD.

The optimization problem is non-convex since we do not assume $A \succcurlyeq 0$, indeed A is required indefinite. However, as anticipated in Section IV, this optimization problem can be solved efficiently even in the case of the non-convexity of the objective (i.e., matrix A is not PSD). Moreover, this is an exceptional case where *strong duality*¹¹ [31] holds, provided that Slater's constraint qualification is fulfilled. That is, there exists an $\mathbf{x} \in \widehat{\mathcal{S}}_m$ such that the inequality constraint (B6b) holds strictly (i.e. not tight). In our case, an example is $\mathbf{x} = \text{vec}_r(\mathbb{I}_m)/\sqrt{m + \epsilon}$ for any $\epsilon > 0$, so $\|\mathbf{x}\|_2^2 < 1$.

Now, we consider the optimization problem consisting of (B6a) and (B6b). We exclude the constraint in (B6c), as we will prove being enforced implicitly by the structure of the matrix A and the non-degeneracy conditions. The Lagrangian function is $\mathcal{L}(\mathbf{x}, \alpha) = \mathbf{x}^\dagger (A + \alpha \mathbb{I}_{m^2}) \mathbf{x} - \alpha$ with the multiplier $\alpha \in \mathbb{R}_+$. Consequently, the dual function $\min_{\mathbf{x}} \mathcal{L}(\mathbf{x}, \alpha)$ takes the value $-\alpha$ when $A + \alpha \mathbb{I}_{m^2} \succcurlyeq 0$

(i.e. PSD, so the Lagrangian is bounded below in \mathbf{x}), and it becomes unbounded otherwise. Let $\lambda_{\min}(\cdot)$ denote the minimum eigenvalue of the matrix argument. The Lagrange dual problem reads

$$\max_{\alpha \in \mathbb{R}_+} -\alpha, \quad (\text{B8a})$$

$$\text{s.t. } A + \alpha \mathbb{I}_{m^2} \succcurlyeq 0, \quad (\text{B8b})$$

then the constraint is fulfilled when $\alpha \geq -\lambda_{\min}(A)$, so the dual optimal is $\alpha^* = -\lambda_{\min}(A) > 0$. The space of the primal solutions is given by the eigenspace corresponding to the minimum eigenvalue of $A - \lambda_{\min}(A) \mathbb{I}_{m^2}$, that is the null space of the latter. Given any matrix A , we denote the null space of A (i.e., the set of solutions of the homogeneous equation $Ax = 0$) by $\text{Null}(A)$. Let

$$\mathbf{x}^* \in \text{Null}(A - \lambda_{\min}(A) \mathbb{I}_{m^2}), \quad (\text{B9})$$

with $\|\mathbf{x}^*\|_2^2 = 1$, be an optimal solution¹², we show that if $\mathbf{x}^* = \text{vec}_r(M)$, then $M = M^\dagger$. That is constraint (B6c) is implied by the structure of matrix A .

The set \mathcal{S}_m of Hermitian matrices of order m is a real vector space, and if \mathcal{B} is a basis for it, then $\mathcal{B}_v := \{\text{vec}_r(K) | K \in \mathcal{B}\}$ is a basis for the vector space of vectorized Hermitians. We verify immediately that, by construction, the image of matrix A belongs to the latter vector space. By the non-degeneracy assumptions (i.e. A is Hermitian indefinite), we have that $\lambda_{\min}(A) \neq 0$. Consequently, the solution \mathbf{x}^* belongs to the image of A , hence the matrix M such that $\text{vec}_r(M) = \mathbf{x}^*$ is Hermitian. In other words, we have shown that the assumption that A is Hermitian indefinite implies that constraint (B6c) is fulfilled. When the non-degeneracy conditions are not met, the case corresponds to the impossibility of obtaining an order parameter (which could be conditioned to the size of the observable). This is a situation we encountered in Section V B.

In (B9) we have proved that the solution may not be unique, however, this is consistent with the non-uniqueness of order parameters stated in Section IV.

We note that even in the case of 1-dimensional null space in (B9), the optimal observable M can be of any rank since the solution \mathbf{x}^* is a vectorization of a Hermitian operator. For example, in the case of the Ising model, we could have $\mathbf{x}^* \approx (1 \ 0 \ 0 \ -1)^\top$ (a Bell's basis vector) with the corresponding observable being $M = \sigma_z$ (full rank).

We summarize the procedure. Given a lattice of RDMs for the ground states of a selected Hamiltonian, we obtain the vector field in (12). The labeling of the phases is obtained using the trigonometric approach explained in Section IV, so we derive the sets I^+ and I^- . Subsequently

⁹ Up to the positive constant (for the objective) $|I^+| \cdot |I^-|$.

¹⁰ As a simple example, this condition is not met when the sets I^+ and I^- are identical. However, this would be incoherent since there is no distinction between the phases.

¹¹ Strong duality is equivalent to the duality gap is zero, that is the difference between primal and dual solutions.

¹² We note that the vectorization operator $\text{vec}_r(\cdot) : \mathbb{C}^{m \times m} \rightarrow \mathbb{C}^{m^2}$ is an isomorphism, so the expression $\mathbf{x}^* = \text{vec}_r(M)$ implicitly means that the matrix M is obtained uniquely from \mathbf{x}^* using the inverse of vec_r .

to the instantiation of matrix A given in (B7), we use its eigendecomposition to obtain, first, the verification that the non-degeneracy conditions are met. Secondly, the eigenspace corresponding to its minimum eigenvalue determines the space of solutions (B9).

We conclude this section with a clarification of the contingency protocol integrated into our method. We begin by assuming that a given QPT is identified via the RFS, enabling the construction of the phase diagram. In accordance with our approach, data from RFS is employed to formulate the optimization problem for the corresponding order parameter. In this study, we focus on linear order parameters, which may, in some cases, be insufficient to distinguish between phases (e.g. topological order). However, the condition on the indefiniteness of the matrix in (B7), ensures a fail-safe mechanism. In other words, we can detect when the linear model is inadequate to capture the phase transition under investigation.

Appendix C: Special solution of the order parameter discovery problem

In this section, we obtain the solution for the special case of the order parameter discovery established by the problem in (16). The outcome is the close form solution put forward in (17).

Fixed the density matrices ρ_+, ρ_- of order m , we define the linear operator $\Xi : \mathcal{S}_m \rightarrow \mathcal{S}_m$ on the space of Hermitian matrices, given by the rule

$$\Xi(K) := -\frac{\langle K, \rho_+ \rangle}{\langle \rho_+, \rho_+ \rangle} \rho_+ + \frac{\langle K, \rho_- \rangle}{\langle \rho_-, \rho_- \rangle} \rho_-, \quad (\text{C1})$$

with $K \in \mathcal{S}_m$. Let $C \in \mathcal{S}_m$ be any non-zero Hermitian, then the operator

$$K \mapsto \frac{\langle K, C \rangle}{\langle C, C \rangle} C \quad (\text{C2})$$

is a projection onto the 1-dimensional subspace spanned by C . Consequently, the operator in (C1) can be related to the *Gram-Schmidt process* (GS) [34]. We obtain the quadratic form for the operator Ξ , so for $K \in \mathcal{S}_m$

$$\langle K, \Xi(K) \rangle = -\frac{\text{Tr}(\rho_+ K)^2}{\text{Tr}(\rho_+^2)} + \frac{\text{Tr}(\rho_- K)^2}{\text{Tr}(\rho_-^2)} \in \mathbb{R}. \quad (\text{C3})$$

The latter is the objective of the problem in (16), so the optimization can be rewritten as

$$\begin{aligned} \min_{M \in \mathcal{S}_m} & \langle M, \Xi(M) \rangle, \\ \text{s.t.} & \|M\|_F^2 \leq 1. \end{aligned} \quad (\text{C4})$$

We obtain the solution of the latter problem by means of the singular value decomposition (SVD) of the operator Ξ , which is established by the following result.

Theorem C.1. *Let $\Xi : \mathcal{S}_n \rightarrow \mathcal{S}_n$ be the linear operator defined in (C1). Assume that for the density matrices ρ_+, ρ_- , defining Ξ , it holds that $\langle \rho_+, \rho_- \rangle \neq 1$. Then,*

$$\Xi(K) = \|V_1\|_F \langle K, \widehat{V}_1 \rangle U_1 + \|U_2\|_F \langle K, V_2 \rangle \widehat{U}_2 \quad (\text{C5})$$

$$= \sqrt{1 - \langle \rho_+, \rho_- \rangle^2} \cdot \left(\langle K, \widehat{V}_1 \rangle U_1 + \langle K, V_2 \rangle \widehat{U}_2 \right) \quad (\text{C6})$$

is the reduced-SVD of Ξ , with non-zero singular values

$$s_1 = s_2 = \sqrt{1 - \langle \rho_+, \rho_- \rangle^2}, \quad (\text{C7})$$

and unnormalized right V_i and left U_i singular vectors

$$V_1 = \widehat{\rho_+} - \langle \rho_+, \widehat{\rho_-} \rangle \widehat{\rho_-}; \quad U_1 = -\widehat{\rho_+}, \quad (\text{C8a})$$

$$V_2 = \widehat{\rho_-}; \quad U_2 = \widehat{\rho_-} - \langle \rho_+, \widehat{\rho_-} \rangle \widehat{\rho_+}. \quad (\text{C8b})$$

Proof. We start by rewriting the operator Ξ defined in (C1) in the equivalent form

$$\Xi(K) = -\langle K, \widehat{\rho_+} \rangle \widehat{\rho_+} + \langle K, \widehat{\rho_-} \rangle \widehat{\rho_-}. \quad (\text{C9})$$

Consider the operator

$$P(K) = \langle K, \widehat{\rho_-} \rangle \langle \widehat{\rho_-}, \widehat{\rho_+} \rangle \widehat{\rho_+}, \quad (\text{C10})$$

then adding and subtracting the latter to Ξ we obtain

$$\begin{aligned} \Xi(K) &= (-\langle K, \widehat{\rho_+} \rangle + \langle K, \widehat{\rho_-} \rangle \langle \widehat{\rho_-}, \widehat{\rho_+} \rangle) \cdot \widehat{\rho_+} \quad (\text{C11a}) \\ &\quad + \langle K, \widehat{\rho_-} \rangle \cdot (\widehat{\rho_-} - \langle \widehat{\rho_-}, \widehat{\rho_+} \rangle \widehat{\rho_+}) \\ &= \langle K, \widehat{\rho_+} - \langle \widehat{\rho_-}, \widehat{\rho_+} \rangle \widehat{\rho_-} \rangle \cdot (-\widehat{\rho_+}) + \langle K, V_2 \rangle U_2 \\ &= \langle K, V_1 \rangle U_1 + \langle K, V_2 \rangle U_2, \end{aligned}$$

with V_i and U_i defined in (C8a). In general, we have that $\langle \rho_+, \rho_- \rangle \neq 0$, so K can have a non-zero projection on both terms of (C9). However, in (C11a) we can immediately verify that $\langle V_1, V_2 \rangle = 0$ and $\langle U_1, U_2 \rangle = 0$. In addition, we verify that

$$\langle V_1, V_1 \rangle = \langle U_2, U_2 \rangle = 1 - \langle \widehat{\rho_+}, \widehat{\rho_-} \rangle^2 \in (0, 1], \quad (\text{C12})$$

thus we can rewrite (C11a) as stated in (C6). Hence, the expression in (C6) is the reduced-SVD of Ξ , as stated in the claim. \square

As the final step, we identify the close formulation for the solution of the problem in (C4), using the SVD of the operator Ξ . We assume the conditions of Theorem C.1. Then, by substituting the right singular vectors into the quadratic form in (C3) we obtain

$$\langle \widehat{V}_1, \Xi(\widehat{V}_1) \rangle = 1 - \frac{\text{Tr}(\rho_+ \rho_-)^2}{\text{Tr}(\rho_+^2)} > 0, \quad (\text{C13a})$$

$$\langle \widehat{V}_2, \Xi(\widehat{V}_2) \rangle = -\left(1 - \langle \widehat{\rho_+}, \widehat{\rho_-} \rangle^2\right) < 0. \quad (\text{C13b})$$

Hence $M = \widehat{V}_2$ (expanded in (17)) is the observable that minimizes the objective in (C3), subject to the norm of the Hermitian M being 1. In Appendix D we showcase the exact formula applied to the Ising model.

Appendix D: Exact example for the order parameter of the Ising model

We consider the quantum Ising model in a transverse magnetic field and the representative density matrices ρ_+, ρ_- for its phases: if the interaction term dominates or the magnetic field strength dominates, respectively. We denote with $\sigma^x, \sigma^y, \sigma^z$ the corresponding Pauli matrices. Let $\rho_+ = \frac{\mathbb{I} + \sigma^z}{2}$ and $\rho_- = \frac{\mathbb{I} - \sigma^x}{2}$. Both ρ_+ and ρ_- are norm 1 orthogonal projections, and $\langle \rho_+, \rho_- \rangle = \frac{1}{2}$. We apply the formula for the optimal observable in (17) to get

$$M^* = \frac{\mathbb{I} + 2\sigma^z - \sigma^x}{2\sqrt{3}} = \frac{\sigma^z}{\sqrt{3}} + \frac{\mathbb{I} - \sigma^x}{2\sqrt{3}} \quad (\text{D1})$$

which is a norm 1 Hermitian. Clearly, for the disordered phase $\text{Tr}(\rho_- M^*) = 0$, whereas $\text{Tr}(\rho_+ M^*) = \frac{\sqrt{3}}{2}$ for the ordered phase. Moreover, we note that M^* is a linear combination of the orthogonal components σ^z and $\mathbb{I} - \sigma^x$. The σ^z operator is the local order parameter or scaling operator, while $\mathbb{I} - \sigma^x$ measures the magnetization in the x -direction.

Now, let $M = \sigma^z / \|\sigma^z\|_F = \sigma^z / \sqrt{2}$ (norm 1 as for M^*), that is the observable M is the magnetization in the z -direction for present model. Then, $\text{Tr}(\rho_- M) = 0$ and $\text{Tr}(\rho_+ M) = \frac{1}{\sqrt{2}}$, hence we confirm that

$$\text{Tr}(\rho_+ M) \leq \text{Tr}(\rho_+ M^*). \quad (\text{D2})$$

In other words, we have shown that the observable M^* presents an increased gap between the phases, when compared to the known magnetization M or it maximizes the value in the order phase.

Appendix E: Experimental Methods

To calculate the ground states for the reduced fidelity susceptibility, we use the density matrix renormalization algorithm (DMRG) [67]. We use two different software packages called Tensor Network Python TENPY [59] and Quantum Simulation with MPS Tensor QS-MPS [68]. In the case of the Rydberg model instead, we use ITENSOR [69].

For the ANNNI model we span the region $(\kappa, h) \in \mathcal{R} = [0.01, 1.5] \times [0.01, 1.5]$ while for the cluster $(K, h) \in \mathcal{R} = [0.5, 1.5] \times [0.5, 1.5]$. We take $n = 64$ points for each axis resulting in a 64×64 lattice of parameters, with a maximum bond dimension $\chi = 64$. Both Hamiltonians in the top-left corner of their respective regions \mathcal{R} are dominated by the σ^z term and thus the states will be a perturbation of the all-up state $|\uparrow\uparrow\cdots\uparrow\rangle$. To ensure the convergence of the DMRG calculations, we use the following strategy: We begin with a region where the states are relatively easy to prepare and where the DMRG converges reliably. From there, we extend the calculation to include nearest-neighbor lattice points, using

the previously obtained state as the initial state. We continue this approach, gradually moving towards regions where states are more challenging to prepare. In doing so, we gain both accuracy and speed. We note the most time-consuming part of the calculation is solving the local eigenvalue problem through the method `eigsh` from the software package SciPY [70]. This procedure is effective up until the point of a phase transition. At that point, if the computation time exceeds a specified threshold (which can be set either arbitrarily or adaptively), we shelve the calculation and proceed to the next lattice point.

Appendix F: The ANNNI model

We first present the phase diagram for the ANNNI Model which is given in Figure 3, where a variety of rich phase transitions are present. We initially begin with small κ and h , where the interactions between neighbors along the x -axis dominate, resulting in a ferromagnetic phase where all spins align parallel to one another, either as $|\rightarrow\rightarrow\cdots\rightarrow\rangle$ or $|\leftarrow\leftarrow\cdots\leftarrow\rangle$. This ferromagnetic region is highlighted in purple in Figure 3.

Upon increasing κ and h , a phase transition occurs as the spins enter a paramagnetic phase (PM), presented in grey in Figure 3. Entering the paramagnetic phase, the transverse magnetic field begins to dominate, causing all states to align with the magnetic field, resulting in the state $|\uparrow\uparrow\cdots\uparrow\rangle$. This Ising-like transition has been previously studied in [40] and the transition line (which corresponds to the purple line in Figure 3) is given in [8, 40] as;

$$h_I \approx \frac{1 - \kappa}{\kappa} \left(1 - \sqrt{\frac{1 - 3\kappa + 4\kappa^2}{1 - \kappa}} \right). \quad (\text{F1})$$

Increasing the parameters h and κ , a further transition becomes evident in the phase diagram between the paramagnetic and floating phases (FP). This incommensurate-incommensurate Kosterlitz-Thouless (KT) phase transition [71–73] (given in blue in Figure 3) has been approximated in [39] to be

$$h_{KT}(\kappa) \approx 1.05 \sqrt{\left(\kappa - \frac{1}{2} \right) (\kappa - 0.1)}. \quad (\text{F2})$$

Such a transition corresponds to a change in the modulation wave vector [74], leading to different incommensurate structures along the spin chain.

A further transition evident in this phase diagram is the transition from the floating phase to the antiphase (AP), where the states exhibit staggered magnetization, as a result of the next-nearest neighbor interactions dominating, corresponding to $|\cdots\leftarrow\rightarrow\leftarrow\leftarrow\cdots\rangle$. Such an incommensurate-commensurate transition (given in green in Figure 3) is described by the Pokrovsky-Talapov

universality class [71, 75], with the transition in this case given by

$$h_{PT} \approx 1.05(\kappa - \frac{1}{2}) \quad (\text{F3})$$

as highlighted in [39] and corresponds to the green line in Figure 3. We also note the presence of the Lifshitz point, marked by a red dot in Figure 3. This point represents a critical point, known as the Lifschitz point (LP), on the phase diagram of certain magnetic systems, where a line of second-order phase transitions meets a line of incommensurate modulated phases [76]. Finally, we note the presence of a disordered line in the ANNNI model, referred to as the Peschel-Every (PE) line [77] within the paramagnetic phase. This line serves as a reference point for understanding the characteristics of this specific phase.

We note this model also reproduces important features observed experimentally in systems that can be described by discrete models with effectively short-range competing interactions [17]. These experimental findings include Lifshitz points [78, 79], adsorbates, ferroelectrics, magnetic systems, and alloys. Conversely, the so-called floating phase emerging in the model is appealing to experimental researchers to explore. This critical incommensurate phase has been observed very recently by using Rydberg-atom ladder arrays [80].

Appendix G: Vector field patterns

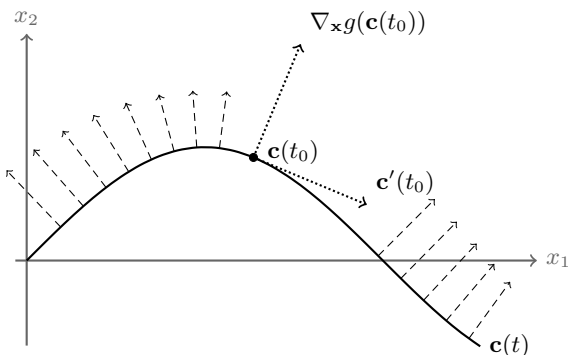


FIG. 17: Curve $\mathbf{c}(t)$ whose image belongs to a level set of a function $g : \mathcal{X} \subseteq \mathbb{R}^2 \rightarrow \mathbb{R}$, that is $g(\mathbf{c}(t))$ is constant for t in some open interval.

This appendix aims to highlight the patterns that emerge in the plot of the vector fields. Specifically, we focus on the "source"-like patterns observed at the phase transitions and the "sink"-like patterns that become evident. We demonstrate the conditions under which these patterns appear in the plot of the vector field $P(\boldsymbol{\lambda})$ (defined in (12)).

Let $g : \mathcal{X} \subseteq \mathbb{R}^n \rightarrow \mathbb{R}$ be a differentiable function and

define the *level set* [81]

$$L(k) := \{\mathbf{x} | \mathbf{x} \in \mathcal{X}, g(\mathbf{x}) = k\} \quad (\text{G1})$$

for some $k \in \mathbb{R}$, as the subset of the domain of g whose image under g is the constant k .

Consider a differentiable curve $\mathbf{c}(t)$ on the level set $L(k)$, that is $\mathbf{c} : I \rightarrow L(k)$ for some open interval $I \subseteq \mathbb{R}$. Consequently, we have that $g(\mathbf{c}(t)) = k$ for all $t \in I$. So, by the chain rule, we obtain

$$\langle \mathbf{c}'(t), \nabla_{\mathbf{x}}g(\mathbf{c}(t)) \rangle = 0, \quad (\text{G2})$$

where $\langle \cdot, \cdot \rangle$ is the inner product on \mathbb{R}^n . In other words, if the vector arguments in (G2) are non-zero, then they must be orthogonal. So, the non-zero gradient of g at a point $\mathbf{c}(t)$ is perpendicular to the tangent of the curve \mathbf{c} at the same point. A pictorial example of the case is given in Figure 17.

We recall that the gradient is the direction of the greatest rate of increase of a function. Then, the source-like structures we observe on the plot of the vector field $P(\boldsymbol{\lambda}) = -\nabla g(\boldsymbol{\lambda})$ (eg. see Figure 9) are the local maxima of the fidelity susceptibility g in the direction transversal to the phase transition. The latter is consistent with the manifestation of QPT as a maxima of the susceptibility in finite-size systems.

Appendix H: Scale invariance of the principal argument

We prove the scale-invariant property of the function $\theta(\boldsymbol{\lambda})$ defined in (13), which is employed in the construction of the phase diagrams.

We begin with a few concepts on the class of homogeneous functions. We call a function $f : K \subseteq \mathbb{R}^n \rightarrow \mathbb{R}$ *positive homogeneous* (PH) of degree α when

$$f(tx) = t^\alpha f(\mathbf{x}) \propto f(\mathbf{x}) \quad (\text{H1})$$

for all scaling factors $t > 0$ such that $tx \in K$. The term "positive" refers to the restriction on the scaling factor $t > 0$, so the degree α can be any real number. The *power law* $x \mapsto c|x|^\alpha$ is PH. The parameter α is known as *critical exponent* in physics. Homogeneity is preserved by differentiation, so for $f : \mathbb{R} \rightarrow \mathbb{R}$

$$\frac{\partial f(tx)}{\partial x} = t f'(tx) = t^\alpha f'(x), \quad (\text{H2})$$

(the right-most equality follows from the definition in (H1)) dividing by t we get $f'(tx) = t^{\alpha-1} f'(x)$ so f' is PH with degree $\alpha - 1$. The latter shows that the vector field in (12) preserves PH. Instead, the angle of the vector field defined in (13) is scale-invariant (when the susceptibility follows the power law as we approach QPT). Indeed, by denoting the partial derivative $g_{\lambda_i} = \partial g / \partial \lambda_i$ of the function g defined in (11), we have that

$$\theta((\boldsymbol{\lambda} - \boldsymbol{\lambda}_c)t) = \arctan \left(\frac{t^{\alpha-1} g_{x_2}(\boldsymbol{\lambda} - \boldsymbol{\lambda}_c)}{t^{\alpha-1} g_{x_1}(\boldsymbol{\lambda} - \boldsymbol{\lambda}_c)} \right) = \theta(\boldsymbol{\lambda} - \boldsymbol{\lambda}_c), \quad (\text{H3})$$

when $g_{x_1}(\boldsymbol{\lambda} - \boldsymbol{\lambda}_c) > 0$ (the other cases for $\text{atan}2(\cdot, \cdot)$ follow similarly), with $\boldsymbol{\lambda}_c$ denoting the critical value for the QPT.

Appendix I: Relation to information geometry

In this appendix, we discuss the fidelity susceptibilities relationship to information geometry and the *Quantum Fisher Information* (QFI). In (2) we introduced the Bures distance as the statistical distance between density matrices. The latter, when considered in terms of a small displacement $d\boldsymbol{\lambda}$ in the vector of parameters $\boldsymbol{\lambda}$, induces the *Bures metric* [82]

$$d_B^2(\rho(\boldsymbol{\lambda}), \rho(\boldsymbol{\lambda} + d\boldsymbol{\lambda})) = \sum_{i,j} h_{\boldsymbol{\lambda}}^{i,j} d\lambda_i d\lambda_j, \quad (\text{I1})$$

where $h_{\boldsymbol{\lambda}}$ is the *metric tensor* at $\boldsymbol{\lambda}$. In other words, the Bures metric is a notion of distinguishability of two density matrices that are infinitesimally close in the coordinate system $\boldsymbol{\lambda}$. In the realm of condensed matter physics, the Bures metric is better known as the fidelity susceptibility (introduced in Section II). Thus, the singularities of the metric $h_{\boldsymbol{\lambda}}$, correspond to the critical regions of the underlying model.

In quantum metrology, the *quantum Cramér-Rao bound* [83, 84], is the quantum equivalent to the classical lower-bound [85] of the variance of the unbiased estimator $\hat{\lambda}$ (i.e. $\mathbb{E}[\hat{\lambda}] = \lambda$) for an unknown parameter λ . The bound, in the case of a single parameter λ , is given by

$$\text{Var}(\hat{\lambda}) \geq \frac{1}{NQ(\rho(\lambda))}, \quad (\text{I2})$$

where N is the number of independent repetitions and $Q(\rho(\lambda))$ is the QFI [82]. We consider a multi-parameter estimator $\hat{\boldsymbol{\lambda}}$ the bound of the covariance matrix becomes

$$\text{Cov}(\hat{\boldsymbol{\lambda}}) \succcurlyeq \frac{Q(\rho(\boldsymbol{\lambda}))^{-1}}{N}, \quad (\text{I3})$$

where the relation $(\cdot) \succcurlyeq (\cdot)$ is the Loewner order (i.e. for $n \times n$ Hermitian matrices A, B , we have that $A \succcurlyeq B$ if and only if $A - B$ is PSD).

There was consensus that, in the general case, the fidelity susceptibility is proportional to the quantum Fisher information [86], that is

$$\mathcal{X}_F(\lambda) \stackrel{?}{=} \frac{1}{4}Q(\rho(\lambda)). \quad (\text{I4})$$

However, in [87] it is proved that at the points where we have a rank change of the density matrix $\rho(\lambda)$, the two quantities are not the same and the QFI presents a discontinuity. We note that the meaning and the consequent violation of the Cramér-Rao theorem on such singularities is still an active area of research [88, 89].

Concerning our formulation, the function $g(\boldsymbol{\lambda})$ defined in (11), can be related directly to the trace of the metric

tensor, that is $g(\boldsymbol{\lambda}) = -\text{Tr}(h_{\boldsymbol{\lambda}})$. The minus factor is used as a convention to make the phase transitions appear as sources in the vector field resulting from (12). In regions of the parameter space \mathcal{X} where the rank of $\rho(\boldsymbol{\lambda})$ is constant, it holds that $g(\boldsymbol{\lambda})$ is proportional to the trace of the QFI matrix. We also note that the trace of $h_{\boldsymbol{\lambda}}$ corresponds to the sum of the susceptibilities for each coupling parameter λ_i . The choice of the trace is also justified by the fact that this operator is basis-independent.

For a comprehensive introduction to information geometry and QPT, we refer to [90].

[1] V. L. Ginzburg and L. D. Landau. On the Theory of superconductivity. *Zh. Eksp. Teor. Fiz.*, 20:1064–1082, 1950.

[2] Leo Kadanoff, Alessandro de angelis, Nicola Giglietto, Sebastiano Stramaglia, M Kibler, and Dennis Dieks. Theories of matter: Infinities and renormalization. *arXiv:1002.2985*, 02 2010.

[3] Leo P. Kadanoff. Relating theories via renormalization. *Studies in History and Philosophy of Science Part B: Studies in History and Philosophy of Modern Physics*, 44(1):22–39, 2013.

[4] Humphrey J. Maris and Leo P. Kadanoff. Teaching the renormalization group. *American Journal of Physics*, 46(6):652–657, 06 1978.

[5] Kerson Huang. A critical history of renormalization. *International Journal of Modern Physics A*, 28(29):1330050, 2013.

[6] Vincent Ardourel and Sorin Bangu. Finite-size scaling theory: Quantitative and qualitative approaches to critical phenomena. *Studies in History and Philosophy of Science*, 100:99–106, 2023.

[7] Saverio Monaco, Oriel Kiss, Antonio Mandarino, Sofia Vallecorsa, and Michele Grossi. Quantum phase detection generalization from marginal quantum neural network models. *Physical Review B*, 107(8), February 2023.

[8] M. Cea, M. Grossi, S. Monaco, E. Rico, L. Tagliacozzo, and S. Vallecorsa. Exploring the phase diagram of the quantum one-dimensional annni model. *arXiv:2402.11022*, 2024.

[9] Teresa Sancho-Lorente, Juan Román-Roche, and David Zueco. Quantum kernels to learn the phases of quantum matter. *Phys. Rev. A*, 105:042432, Apr 2022.

[10] Julian Arnold, Frank Schäfer, Alan Edelman, and Christoph Bruder. Mapping out phase diagrams with generative classifiers. *Phys. Rev. Lett.*, 132:207301, May 2024.

[11] Julian Arnold and Frank Schäfer. Replacing neural networks by optimal analytical predictors for the detection of phase transitions. *Phys. Rev. X*, 12:031044, Sep 2022.

[12] Richard Jozsa. Fidelity for mixed quantum states. *Journal of Modern Optics*, 41(12):2315–2323, 1994.

[13] Amit Dutta, Gabriel Aeppli, Bikas K. Chakrabarti, Uma Divakaran, Thomas F. Rosenbaum, and Diptiman Sen. *Quantum Phase Transitions in Transverse Field Spin Models: From Statistical Physics to Quantum Information*. Cambridge University Press, 2015.

[14] Shi-Jian Gu. Fidelity approach to quantum phase transitions. *International Journal of Modern Physics B*, 24(23):4371–4458, September 2010.

[15] Wen-Long You, Ying-Wai Li, and Shi-Jian Gu. Fidelity, dynamic structure factor, and susceptibility in critical phenomena. *Phys. Rev. E*, 76:022101, Aug 2007.

[16] Jiannis K. Pachos and Martin B. Plenio. Three-spin interactions in optical lattices and criticality in cluster hamiltonians. *Phys. Rev. Lett.*, 93:056402, Jul 2004.

[17] Walter Selke. The annni model — theoretical analysis and experimental application. *Physics Reports*, 170:213–264, 1988.

[18] Natalia Chepiga and Frédéric Mila. Lifshitz point at commensurate melting of chains of rydberg atoms. *Phys. Rev. Res.*, 3:023049, Apr 2021.

[19] Xue-Jia Yu, Sheng Yang, Jing-Bo Xu, and Limei Xu. Fidelity susceptibility as a diagnostic of the commensurate-incommensurate transition: A revisit of the programmable rydberg chain. *Phys. Rev. B*, 106:165124, Oct 2022.

[20] Rhine Samajdar, Soonwon Choi, Hannes Pichler, Mikhail D. Lukin, and Subir Sachdev. Numerical study of the chiral F_3 quantum phase transition in one spatial dimension. *Phys. Rev. A*, 98:023614, Aug 2018.

[21] Jose Carrasco, Andreas Elben, Christian Kokail, Barbara Kraus, and Peter Zoller. Theoretical and experimental perspectives of quantum verification. *PRX Quantum*, 2:010102, Mar 2021.

[22] Michael A. Nielsen and Isaac L. Chuang. *Quantum Computation and Quantum Information: 10th Anniversary Edition*. Cambridge University Press, USA, 10th edition, 2011.

[23] Armin Uhlmann. The "transition probability" in the state space of a $*$ -algebra. *Reports on Mathematical Physics*, 9:273–279, 1976.

[24] E. Schrödinger. Quantisierung als Eigenwertproblem. *Annalen Phys.*, 384(4):361–376, 1926.

[25] Lei Wang, Ye-Hua Liu, Jakub Imriška, Ping Nang Ma, and Matthias Troyer. Fidelity susceptibility made simple: A unified quantum monte carlo approach. *Physical Review X*, 5(3), July 2015.

[26] Paulo E. M. F. Mendonça, Reginaldo d. J. Napolitano, Marcelo A. Marchiolli, Christopher J. Foster, and Yeong-Cherng Liang. Alternative fidelity measure between quantum states. *Physical Review A*, 78(5), November 2008.

[27] Paolo Zanardi, H. T. Quan, Xiaoguang Wang, and C. P. Sun. Mixed-state fidelity and quantum criticality at finite temperature. *Phys. Rev. A*, 75:032109, Mar 2007.

[28] Paolo Zanardi, Lorenzo Campos Venuti, and Paolo Giorda. Bures metric over thermal state manifolds and quantum criticality. *Phys. Rev. A*, 76:062318, Dec 2007.

[29] A. Fabricio Albuquerque, Fabien Alet, Clément Sire, and Sylvain Capponi. Quantum critical scaling of fidelity susceptibility. *Phys. Rev. B*, 81:064418, Feb 2010.

[30] Shunsuke Furukawa, Grégoire Misguich, and Masaki Oshikawa. Systematic derivation of order parameters through reduced density matrices. *Phys. Rev. Lett.*, 96:047211, Feb 2006.

[31] Stephen Boyd and Lieven Vandenberghe. *Convex Optimization*. Cambridge University Press, 2004.

[32] Andrew R. Conn, Nicholas I. M. Gould, and Philippe L. Toint. *Trust Region Methods*. Society for Industrial and Applied Mathematics, 2000.

[33] Franz Rendl and Henry Wolkowicz. A semidefinite framework for trust region subproblems with applications to large scale minimization. *Mathematical Programming*, 77(1):273–299, Apr 1997.

[34] Gene H. Golub and Charles F. Van Loan. *Matrix computations (3rd ed.)*. Johns Hopkins University Press, USA, 1996.

[35] N. Goldenfeld. *Lectures On Phase Transitions And The Renormalization Group*. CRC Press, 1992.

[36] R. J. Elliott. Phenomenological discussion of magnetic ordering in the heavy rare-earth metals. *Phys. Rev.*, 124:346–353, Oct 1961.

[37] Michael E. Fisher and Walter Selke. Infinitely many commensurate phases in a simple ising model. *Phys. Rev. Lett.*, 44:1502–1505, Jun 1980.

[38] Anjan Kumar Chandra and Subinay Dasgupta. Floating phase in a 2D ANNNI model. *Journal of Physics A Mathematical General*, 40(24):6251–6265, June 2007.

[39] Matteo Beccaria, Massimo Campostrini, and Alessandra Feo. Evidence for a floating phase of the transverse annni model at high frustration. *Phys. Rev. B*, 76:094410, Sep 2007.

[40] Sei Suzuki, Jun-ichi Inoue, and Bikas K. Chakrabarti. *Quantum Ising Phases and Transitions in Transverse Ising Models*. Springer Berlin Heidelberg, Berlin, Heidelberg, 2013.

[41] Anjan Kumar Chandra and Subinay Dasgupta. Floating phase in the one-dimensional transverse axial next-nearest-neighbor ising model. *Phys. Rev. E*, 75:021105, Feb 2007.

[42] P.H. Lundow and I.A. Campbell. The ising universality class in dimension three: Corrections to scaling. *Physica A: Statistical Mechanics and its Applications*, 511:40–53, 2018.

[43] Raúl Morral-Yepes, Frank Pollmann, and Izabella Lovasz. Detecting and stabilizing measurement-induced symmetry-protected topological phases in generalized cluster models. *Phys. Rev. B*, 108:224304, Dec 2023.

[44] David Perez-Garcia, M Wolf, Mikel Sanz, Frank Verstraete, and J Cirac. String order and symmetries in quantum spin lattices. *Physical Review Letters*, 100:167202, 04 2008.

[45] Adam Smith, Bernhard Jobst, Andrew G. Green, and Frank Pollmann. Crossing a topological phase transition with a quantum computer. *Phys. Rev. Res.*, 4:L022020, Apr 2022.

[46] Hannes Bernien, Sylvain Schwartz, Alexander Keesling, Harry Levine, Ahmed Omran, Hannes Pichler, Soonwon Choi, Alexander S Zibrov, Manuel Endres, Markus Greiner, et al. Probing many-body dynamics on a 51-atom quantum simulator. *Nature*, 551(7682):579–584, 2017.

[47] Hannes Bernien, Sylvain Schwartz, Alexander Keesling, Harry Levine, Ahmed Omran, Hannes Pichler, Soonwon Choi, Alexander S. Zibrov, Manuel Endres, Markus Greiner, Vladan Vuletić, and Mikhail D. Lukin. Probing many-body dynamics on a 51-atom quantum simulator. *Nature*, 551(7682):579–584, 2017.

[48] Dolev Bluvstein, Simon J. Evered, Alexandra A. Geim, Sophie H. Li, Hengyun Zhou, Tom Manovitz, Sepehr Ebadi, Madelyn Cain, Marcin Kalinowski, Dominik Hangleiter, J. Pablo Bonilla Ataides, Nishad Maskara, Iris Cong, Xun Gao, Pedro Sales Rodriguez, Thomas Karolyshyn, Giulia Semeghini, Michael J. Gullans, Markus Greiner, Vladan Vuletić, and Mikhail D. Lukin. Logical quantum processor based on reconfigurable atom arrays. *Nature*, 626(7997):58–65, 2024.

[49] Iris Cong, Harry Levine, Alexander Keesling, Dolev Bluvstein, Sheng-Tao Wang, and Mikhail D. Lukin. Hardware-efficient, fault-tolerant quantum computation with rydberg atoms. *Phys. Rev. X*, 12:021049, Jun 2022.

[50] Quantum information with rydberg atoms. *Reviews of modern physics*, 82(3):2313–2363, 2010.

[51] Antoine Browaeys and Thierry Lahaye. Many-body physics with individually controlled rydberg atoms. *Nature Physics*, 16(2):132–142, 2020.

[52] Jonathan Z. Lu, Rodrigo Araiza Bravo, Kaiying Hou, Gebremedhin A. Dagnew, Susanne F. Yelin, and Khadijeh Najafi. Learning quantum symmetries with interactive quantum-classical variational algorithms. *J. Phys. A*, 57(31):315304, 2024.

[53] Antoine Browaeys and Thierry Lahaye. Many-body physics with individually controlled Rydberg atoms. *Nature Physics*, 16(2):132–142, January 2020.

[54] Natalia Chepiga and Frédéric Mila. Kibble-zurek exponent and chiral transition of the period-4 phase of rydberg chains. *Nature Communications*, 12, 01 2021.

[55] Alioscia Hamma, Radu Ionicioiu, and Paolo Zanardi. Bipartite entanglement and entropic boundary law in lattice spin systems. *Physical Review A*, 71(2), February 2005.

[56] Michael Levin and Xiao-Gang Wen. Detecting topological order in a ground state wave function. *Physical Review Letters*, 96(11), March 2006.

[57] Alexei Kitaev and John Preskill. Topological entanglement entropy. *Physical Review Letters*, 96(11), March 2006.

[58] U. Schollwöck. The density-matrix renormalization group. *Rev. Mod. Phys.*, 77:259–315, Apr 2005.

[59] Johannes Haensch and Frank Pollmann. Efficient numerical simulations with Tensor Networks: Tensor Network Python (TeNPy). *SciPost Phys. Lect. Notes*, page 5, 2018. Code available from <https://github.com/tenpy/tenpy>.

[60] Irwin Sobel. An isotropic 3x3 image gradient operator. *Presentation at Stanford A.I. Project 1968*, 02 2014.

[61] Larry S. Davis. A survey of edge detection techniques. *Computer Graphics and Image Processing*, 4(3):248–270, 1975.

[62] Peter Kovesi. Good colour maps: How to design them. *arXiv:1002.2985*, 2015.

[63] J. D. Hunter. Matplotlib: A 2d graphics environment. *Computing in Science & Engineering*, 9(3):90–95, 2007.

[64] F.J. Harris. *Multirate Signal Processing for Communication Systems*. Prentice Hall PTR, 2004.

[65] J.C. Butcher. A history of runge-kutta methods. *Applied Numerical Mathematics*, 20(3):247–260, 1996.

[66] Roger A. Horn and Charles R. Johnson. *Matrix Analysis*. Cambridge University Press, USA, 2nd edition, 2012.

[67] Ulrich Schollwöck. The density-matrix renormalization group in the age of matrix product states. *Annals of Physics*, 326(1):96–192, January 2011.

[68] Francesco Di Martantonio. Quantum simulation with mps tensor, 2024. Code available from <https://github.com/Fradm98/qs-mps>.

[69] Matthew Fishman, Steven White, and Edwin Stoudenmire. The itensor software library for tensor network calculations. *SciPost Physics Codebases*, August 2022.

[70] Pauli Virtanen, Ralf Gommers, Travis E. Oliphant, Matt Haberland, Tyler Reddy, David Cournapeau, Evgeni Burovski, Pearu Peterson, Warren Weckesser, Jonathan Bright, Stéfan J. van der Walt, Matthew Brett, Joshua Wilson, K. Jarrod Millman, Nikolay Mayorov, Andrew R. J. Nelson, Eric Jones, Robert Kern, Eric Larson, C J Carey, İlhan Polat, Yu Feng, Eric W. Moore, Jake VanderPlas, Denis Laxalde, Josef Perktold, Robert Cimrman, Ian Henriksen, E. A. Quintero, Charles R. Harris, Anne M. Archibald, António H. Ribeiro, Fabian Pedregosa, Paul van Mulbregt, and SciPy 1.0 Contributors. SciPy 1.0: Fundamental Algorithms for Scientific Com-

puting in Python. *Nature Methods*, 17:261–272, 2020.

[71] V. L. Pokrovsky and A. L. Talapov. Ground state, spectrum, and phase diagram of two-dimensional incommensurate crystals. *Phys. Rev. Lett.*, 42:65–67, Jan 1979.

[72] David A. Huse and Michael E. Fisher. Commensurate melting, domain walls, and dislocations. *Phys. Rev. B*, 29:239–270, Jan 1984.

[73] P. Bak. Review Article: Commensurate phases, incommensurate phases and the devil's staircase. *Reports on Progress in Physics*, 45(6):587–629, June 1982.

[74] Ruben Verresen, Ashvin Vishwanath, and Frank Pollmann. Stable Luttinger liquids and emergent $U(1)$ symmetry in constrained quantum chains. *arXiv e-prints*, page arXiv:1903.09179, March 2019.

[75] Y.-J. Wang, F. H. L. Essler, M. Fabrizio, and A. A. Nersesyan. Quantum criticalities in a two-leg antiferromagnetic $s = \frac{1}{2}$ ladder induced by a staggered magnetic field. *Phys. Rev. B*, 66:024412, Jul 2002.

[76] A.K. Murtazaev and J.G. Ibaev. Critical properties of an annni-model in the neighborhood of multicritical lifshitz point. *Solid State Communications*, 152:177–179, 02 2012.

[77] I Peschel and V J Emery. Calculation of spin correlations in two-dimensional ising systems from one-dimensional kinetic models. *Zeitschrift für Physik B Condensed Matter*, 43(3):241–249, September 1981.

[78] Malte Henkel and Michel Pleimling. *Lifshitz Points: Strongly Anisotropic Equilibrium Critical Points*, pages 337–368. Springer Netherlands, Dordrecht, 2010.

[79] R.M. Hornreich. The lifshitz point: Phase diagrams and critical behavior. *Journal of Magnetism and Magnetic Materials*, 15-18:387–392, 1980.

[80] Jin Zhang et al. Probing quantum floating phases in Rydberg atom arrays. *arXiv: 2401.08087*, 1 2024.

[81] T.M. Apostol. *Calculus. Vol. II: Multi-variable Calculus and Linear Algebra, with Applications to Differential Equations and Probability*. Number v. 2 in Blaisdell international textbook series. Xerox College Publ., 1969.

[82] Matteo G. A. Paris. Quantum estimation for quantum technology. *International Journal of Quantum Information*, 07(supp01):125–137, 2009.

[83] Carl W. Helstrom. Quantum detection and estimation theory. *Journal of Statistical Physics*, 1(2):231–252, 1969.

[84] Samuel L. Braunstein and Carlton M. Caves. Statistical distance and the geometry of quantum states. *Phys. Rev. Lett.*, 72:3439–3443, May 1994.

[85] C. Radhakrishna Rao. *Information and the Accuracy Attainable in the Estimation of Statistical Parameters*, pages 235–247. Springer New York, New York, NY, 1992.

[86] Jing Liu, Heng-Na Xiong, Fei Song, and Xiaoguang Wang. Fidelity susceptibility and quantum fisher information for density operators with arbitrary ranks. *Physica A: Statistical Mechanics and its Applications*, 410, 01 2014.

[87] Dominik Šafránek. Discontinuities of the quantum fisher information and the bures metric. *Phys. Rev. A*, 95:052320, May 2017.

[88] Luigi Seveso, Francesco Albarelli, Marco G Genoni, and Matteo G A Paris. On the discontinuity of the quantum fisher information for quantum statistical models with parameter dependent rank. *Journal of Physics A: Mathematical and Theoretical*, 53(2):02LT01, dec 2019.

[89] A. T. Rezakhani, M. Hassani, and S. Alipour. Continuity of the quantum fisher information. *Phys. Rev. A*, 100:032317, Sep 2019.

[90] Paolo Zanardi, Paolo Giorda, and Marco Cozzini. Information-theoretic differential geometry of quantum phase transitions. *Phys. Rev. Lett.*, 99:100603, Sep 2007.